Integrative Biology

Accepted Manuscript

Volume 8 | Number 1 | January 2016 | Pages 1–122

Integrative Biology

Interdisciplinary approaches for molecular and cellular life sciences
www.rsc.org/biology

ISSN 1757-9694

ROYAL SOCIETY OF CHEMISTRY

PAPER
Peggy P. Y. Chan et al
Assessment of the potential of a high frequency acoustomicrofluidic nebulisation platform for inhaled stem cell therapy

Indexed in Medline!

This is an Accepted Manuscript, which has been through the Royal Society of Chemistry peer review process and has been accepted for publication.

Accepted Manuscripts are published online shortly after acceptance, before technical editing, formatting and proof reading. Using this free service, authors can make their results available to the community, in citable form, before we publish the edited article. We will replace this Accepted Manuscript with the edited and formatted Advance Article as soon as it is available.

You can find more information about Accepted Manuscripts in the author guidelines.

ROYAL SOCIETY OF CHEMISTRY

rsc.li/integrative-biology

Insight, Innovation and Integration

Re-epithelialization is one of the fundamental steps in wound healing process, in which epithelial keratinocytes migrate laterally to cover the denuded area of a wound in response to epidermal growth factor (EGF) secreted by nearby dermal fibroblasts. While it is widely known that EGF can stimulate cell migration via increased integrin expression, there are also studies suggesting that high EGF concentration causes keratinocyte migration to decelerate, contributing to delayed re-epithelialization and subsequently chronic non-healing wounds. Our mathematical model presents a novel approach to study keratinocyte migration influenced by EGF secreted by fibroblasts through paracrine signaling giving rise to the delayed re-epithelialization. The model provides insight into our understanding of integrin-mediated cell migration in wound healing, as well as other physiological and pathological events.

ROYAL SOCIETY
OF CHEMISTRY

Journal Name

ARTICLE TYPE

Computational model of wound healing: EGF secreted by fibroblasts promotes delayed re-epithelialization of epithelial keratinocytes[†]

Vivi Andasari[*a], Dongyuan Lü[b], Maciej Swat[c], ShiLiang Feng[b], Fabian Spill[a], Li Chen[d], Xiangdong Luo[d], Muhammad Zaman[a], and Mian Long[b]

It is widely agreed that keratinocyte migration plays a crucial role in wound re-epithelialization. Defects in this function contribute to wound reoccurrence causing significant clinical problems. Several *in vitro* studies have shown that the speed of migrating keratinocytes can be regulated by epidermal growth factor (EGF) which affects keratinocyte's integrin expression. The relationship between integrin expression (through cell-matrix adhesion) stimulated by EGF and keratinocyte migration speed is not linear since increased adhesion, due to increased integrin expression, has been experimentally shown to slow down cell migration due to the biphasic dependence of cell speed on adhesion. In our previous work we showed that keratinocytes that were co-cultured with EGF-enhanced fibroblasts formed an asymmetric migration pattern, where, the cumulative distances of keratinocytes migrating toward fibroblasts were smaller than those migrating away from fibroblasts. This asymmetric pattern is thought to be provoked by high EGF concentration secreted by fibroblasts. The EGF stimulates the expression of integrin receptors on the surface of keratinocytes migrating toward fibroblasts via paracrine signaling. In this paper, we present a computational model of keratinocyte migration that is controlled by EGF secreted by fibroblasts using the Cellular Potts Model (CPM). Our computational simulation results confirm the asymmetric pattern observed in experiments. These results provide a deeper insight into our understanding of the complexity of keratinocyte migration in the presence of growth factor gradients and may explain re-epithelialization failure in impaired wound healing.

1 Introduction

Based on the time frame of healing, wounds are classified into: (i) acute wounds, or wounds that repair themselves normally in a timely and efficient manner with the end result of functional and aesthetic restoration, and (ii) chronic wounds, or wounds that fail to progress through the normal stages of healing, resulting in delayed and incomplete healing process[1]. Non-healing wounds can have a poor clinical outcome and subsequent economic impact.

In the United States alone, chronic non-healing wounds prompt enormous expenditures with an estimated cost that exceeds $50 billion per year for caring for these wounds[2]. Recent advances in cellular and molecular biology have immensely broadened our understanding of complex processes involved in wound healing. The optimal wound healing phases, which are highly programmed, include a series of steps, such as: (i) rapid hemostasis by vascular constriction and fibrin clot formation which both begin immediately after wounding, (ii) appropriate inflammation through chemotaxis by white blood cells, (iii) mesenchymal cell differentiation, proliferation, and migration to the wound site, (iv) angiogenesis, (v) re-epithelialization, which includes re-growth and migration of epithelial keratinocytes in the epidermal layer over the wound surface, and (vi) synthesis, cross-linking, and collagen alignment for tissue strength[3]. All these phases must occur in the proper sequence and a regulated manner for successful wound healing. Wounds that are healed appropriately are commonly parameterized by the re-epithelialization phase[4,5], from which, tissue integrity and normal functions can be fully restored rapidly and efficiently. On the other hand, de-

[a] *Boston University, Department of Biomedical Engineering, 44 Cummington Mall, Boston MA 02215, USA. E-mail: andasari@bu.edu*

[b] *Chinese Academy of Sciences, Key Laboratory of Microgravity (National Microgravity Laboratory), Center of Biomechanics and Bioengineering, and Beijing Key Laboratory of Engineered Construction and Mechanobiology, Institute of Mechanics, Beijing, 100190, China.*

[c] *University of Pennsylvania, Computational Memory Lab, Philadelphia, MA, 19104, USA.*

[d] *Third Military Medical University, Burn Research Institute, Southwest Hospital, Chongqing, 400038, China.*

Integrative Biology Accepted Manuscript

fects in this process can contribute to the formation of wound reoccurrence and chronic non-healing wounds, which are significant clinical problems[6]. For this reason, a better understanding of re-epithelialization is crucial for developing new therapeutic approaches for successful wound healing and its acceleration.

Re-epithelialization is a process of covering the denuded area of a wound. It involves migration and proliferation of epidermal keratinocyte cells, with migration being the earlier event that takes place. Numerous studies carried out since at least the last four decades suggest that keratinocyte migration and proliferation in re-epithelialization are stimulated by a number of cytokines and growth factors (reviewed in[7–11]), such as the families of epidermal growth factor (EGF)[12–17], transforming growth factor-β (TGF-β)[18,19], fibroblast growth factor (FGF)[20,21], keratinocyte growth factor (KGF)[22,23], and insulin growth factor-1 (IGF-1)[15,24–26]. Some of these growth factors play a significant role in the stimulation of cell surface adhesion receptors responsible for cell migration, i.e., integrins, which are crucially important for keratinocyte migration through autocrine, paracrine, or endocrine signaling. For example, TGF-β_1 induces the expression of integrin subunits α_5, α_v, and β_5 which facilitate re-epithelialization of a porcine cutaneous wound model[27]. Aside from modulating integrins β_1 and β_5, TGF-β_1 also up-regulates de novo expression of integrin $\alpha_v\beta_6$ in human epidermal keratinocytes[28]. Similarly, EGF promotes human keratinocyte migration by increasing the expression of integrin subunit α_2[29]. Integrin $\alpha_6\beta_4$ expression is regulated by EGF in rabbit corneal epithelial cells[30]. In mouse keratinocyte cells, both EGF and hepatocyte growth factor (HGF) stimulate chemokinetic (random) and chemotactic (directional) migration on type I collagen- and fibronectin-coated substrates mediated by integrin β_1 via PI3K and MEK/ERK pathways[31]. In human keratinocytes, integrin β_1 influences cell migration via PI3K and ERK pathways[32].

Although in those studies growth factors are asserted as a stimulator for keratinocyte migration, there are reports unveiling the opposite, in which growth factors are also implicated in delayed re-epithelialization or decreased keratinocyte migration, rendering chronic non-healing wounds. Abundant expression of TGF-β was observed in chronic non-healing wounds in a mouse model, concentrated in a connective tissue underneath epithelial cells with strongly up-regulated integrin $\alpha_v\beta_6$ expression[33,34]. Other studies also reveal that high levels of EGF concentration evince a downward trend in accumulative keratinocyte migration speed[16,29,35,36]. The underlying molecular and cellular mechanisms of the EGF-dependent keratinocyte deceleration speed have yet been largely explored and investigated. Nevertheless, in our previous work[37] we showed that migrating keratinocytes exhibited an asymmetric pattern of migration when the cells were co-cultured with fibroblasts whose EGF secretion was enhanced using a static mechanical stretch. The cumulative distances of keratinocytes moving away from fibroblasts were longer than those of keratinocytes moving toward fibroblasts. We hypothesized that keratinocytes moving toward fibroblasts perceive high gradient of EGF stimulating integrin activation and expression necessary for keratinocyte migration. However, if the EGF concentration is too high, integrin expression becomes strongly up-regulated leading

to keratinocyte's deceleration. It turns out that the hypothesis on the relation between EGF (ligand) levels and integrin expression is supported by a number of experimental studies. These studies confirm that integrins and EGF are important participants in cell migration, in which EGF is considered to play a big role in enhancing integrin cell-surface expression and activity[38–47]. It should be noted that, EGF up-regulates the expression of integrin in a dose-dependent manner[14,45]. Furthermore, integrin cell-surface expression was observed to be up-regulated by high EGF treatment, and this up-regulation was not observed under a relatively low EGF concentration[40]. It has been confirmed that the up-regulation of EGF and it's receptors responsible for integrin function is the initiation of integrin intracellular signaling pathway by PI3-K[48]. Therefore, in our model, keratinocyte asymmetric migration is thought to be triggered by high EGF concentration secreted by fibroblasts that stimulates the expression of integrin on keratinocytes migrating toward fibroblasts.

In integrin-mediated lateral cell migration (on 2D substrates), the levels of integrin expression are correlated with the size and protein composition of adhesion structures. Cell migration speed is high at small adhesions and as adhesions grow bigger and become mature, which is related to high integrin expressions, cell speed decelerates and cells are eventually prevented from moving forward when adhesions are large and stable[49,50]. This phenomenon is deemed as a biphasic dependence of keratinocyte migration speed on integrin expression, in which cell migration speed accelerates as integrin expression increases and the speed is optimum at a certain level of integrin expression[51]. Past the critical integrin expression level, migration speed decreases to a stop. Such biphasic behavior has been observed in numerous experimental studies. For example, the speed of Chinese hamster ovary (CHO) cells that migrate on fibronectin is optimal at intermediate levels of $\alpha_5\beta_1$ expression[52] and human breast carcinoma cell line (T47D) motility on collagen types I and IV is maximal at an intermediate level of $\alpha_2\beta_1$ expression[53]. Aside from integrin expression, other components of cell migration such as ligand concentration, integrin-ligand binding affinity, and growth factors can also generate a biphasic response[51,54–58]. The biphasic dependence of cell speed on these aspects has been studied theoretically[59–63]. Another experiment presented in this paper supports this hypothesis, that integrin β_1 expression is stronger in epidermal cells closer to the dermis layer than in distant areas. It is important to note that fibroblasts, the major component of the dermis layer, synthesize EGF or IGF-1 which induces keratinocyte migration via paracrine signaling[11].

Motivated by these experimental studies, in this paper we present a computational model of keratinocyte migration influenced by EGF secreted by fibroblasts through paracrine signaling. We apply the Cellular Potts Model (CPM), also known as the Glazier-Graner-Hogeweg (GGH) model, for keratinocyte migration influenced by EGF. Our model is based on effective adhesion energy for the regulation of migration due to integrin expression governed by EGF diffusion and secretion and integrin-ligand binding affinity. We assume that EGF only affects integrin expression, whereas the expression of other adhesion molecules, such as Immunoglobulin superfamily molecules, cadherins, selectins,

is not influenced by EGF. In our model, keratinocytes migrating toward fibroblasts perceive gradient concentration of EGF via either diffusion or secretion, such that if the EGF concentration perceived by keratinocytes increases, their integrin expression also increases. Combined with integrin-ligand binding affinity, the persistent increase in integrin expression leads to changes in cell surface tension, which, above some threshold value, initiates the down-regulation of keratinocyte movement. Keratinocytes at the other end (those migrating away from fibroblasts) are not influenced by EGF, and their integrin expression and migration are not affected or remain steady. The difference in the migrating distances leads to what we call here the asymmetric migration pattern. If EGF diffuses rapidly or if it is overly secreted, it impedes keratinocyte migration and creates asymmetric pattern at early stages/days. The computational simulation results of our model with chosen parameter values show aligned comparison with experimental studies. Our study may provide new insights into the re-epithelialization process, such that, depending on its diffusion and secretion, EGF can either accelerate or decelerate the covering of denuded epithelial layer, the latter may cause delayed re-epithelialization and subsequently provoke impaired wound healing, creating chronic non-healing wounds.

2 Materials and Methods

2.1 The Experiments

The re-epithelialization phase is accomplished by lateral movement of keratinocyte cells from the wound edge onto the wound provisional matrix, forming a ring of re-epithelialization that progresses toward the wound center[64]. In our previous study (Lü et al 2012), from which our mathematical model is based on, we measured migrating distances of immortalized human keratinocytes (HaCaT) and human dermal fibroblasts (HF) from three conditions: (i) fibroblast monocultures, (ii) keratinocyte monocultures, and (iii) fibroblast/keratinocyte co-cultures. In order to see if high concentration of EGF would affect keratinocyte and fibroblast migration, another set of experiments with the same conditions was performed in which static mechanical stretch was applied once at the beginning of experiments. The mechanical stretch was intended to enhance EGF secretion, either by fibroblasts or keratinocytes. The secretion of EGF was tested using an ELISA assay and daily secretion of the mean EGF content was shown in Figure 1. From the figure, we can observe that applying mechanical stretch indeed enhanced the EGF content of fibroblast monocultures (yellow bar) and fibroblast/keratinocyte co-cultures (green bar). The optical density (OD) was measured at a wavelength of 450 nm by an automated ELISA reader (Bio-rad iMark template reader, Bio-rad, USA) to detect the level of EGF expression. The value of OD450 is proportional to the amount of protein expression.

In all six conditions, a rectangular shaped of tensile device, sized 20×42 mm, was used. The device was mainly composed of an elastic (made of poly-dimethylsiloxane or PDMS) membrane, for a maximum of 30% strain of mechanical stretch, which was coated with type I collagen. For monoculture tests each cell type was seeded at the center of the membrane, whereas, for co-

culture tests keratinocyte and fibroblast cells were seeded abreast with a ~ 8 mm gap between the two cell types, as shown by the right (monoculture setup) and left (co-culture setup) of Figure 2. This setup was aimed at representing keratinocyte lateral migration, as normally occurs in the re-epithelialization of wound healing. Without going into detail on how keratinocytes and fibroblasts are distributed in the epidermal and dermal layers of the skin, this setup was also meant for studying the paracrine effect of EGF secreted by fibroblasts on the lateral migration of keratinocytes.

Cell migration was monitored using a CCD-camera in a time interval of ~ 24 hours for six days. Cell migration distance was estimated from the position of cells at the front of the popula-tion and measured along the long-axis of the PDMS membrane. In co-culture conditions, keratinocyte cells were placed on the left side of fibroblasts. The average global cell displacement was observed daily, with different accumulative distances measured each day. We classify the monitored keratinocyte displacement re-sults in four cases: (i) non-stretched monocultures, (ii) stretched monocultures, (iii) non-stretched co-cultures, and (iv) stretched co-cultures. Cells on the outer layers of keratinocyte group migrated to the right or toward fibroblasts (green curves) and to the left or away from fibroblasts (orange curves) as shown by the daily average cumulative displacement data in Figure 3.

Since we were only interested in cell migration, the effect of cell proliferation on migration was eliminated to avoid the confluence of keratinocytes and fibroblasts. To inhibit cell proliferation, both cell types were initially exposed to 10 μg/ml mitomycin C for 2 hours. Mitomycin C is a potent DNA crosslinker that can cause the depolymerization of DNA and hinder the replication of DNA, thus inhibiting cell division. We then used MTT cell proliferation assay to examine the inhibition efficiency of cells. This optimized treatment condition ensured that cell proliferation was effectively suppressed within six days. When the experiment ended on the 6th day, both fibroblasts and keratinocytes migrated toward fibroblasts were not confluent but located very close.

The experimental results show that the curves eliciting cumulative distances between keratinocytes moving toward fibroblasts (green) and keratinocytes moving away from fibroblasts (orange) are similar in trend for non-stretched monocultures (Figure 3a), stretched monocultures (Figure 3b), and non-stretched co-cultures (Figure 3c) cases. In the stretched co-cultures case (Figure 3d), the cumulative migration distance of keratinocytes moving away from fibroblasts was significantly higher than that when moving toward fibroblasts. In other cases (non-stretched and stretched monocultures), although there seems to be a little asymmetry between migration to the left and to the right, there is no statistically significant difference between the left and right groups ($P > 0.05$), and the cumulative migration distance of keratinocytes moving toward fibroblasts was much lower than that when moving away from fibroblasts. The migrating distance differences start after day 2 and are more noticeable after day 4. As seen in Figure 1 where the stretched co-culture condition has the highest mean EGF content, it is sensible to deduce that the differences of migrating distance in Figure 3d are due to high EGF concentration, secreted mainly by fibroblasts. Keratinocytes

moving away from fibroblasts (orange line) perceived high concentration of EGF, hence they migrated fast and traveled almost 7 mm on day 6, whereas keratinocytes in other conditions (a, b, and c) barely reached 6 mm on the same day. However, for keratinocytes moving toward fibroblasts (green line), where it is evident that they perceived very high EGF from fibroblasts which were located across the gap that was getting narrower as they kept moving forward, it is possible that the keratinocytes reached a limit of excessive high concentration of EGF which can saturate cell-matrix adhesion via integrin expression and decelerate movement. These findings suggest that there may be a connection between cellular properties of keratinocytes affected by EGF and the location of keratinocytes with respect to fibroblasts, all impacting cell migration speed.

Another *in vivo* experiment we performed appears to support the suggestion above, that, keratinocytes in the epidermal layer that were located close to fibroblasts in the dermal layer had a distinct cellular property, where they expressed higher integrin β_1 than keratinocytes located further away from fibroblasts. The result, shown in Figure 4, exhibited an uneven distribution of integrin β_1 in epidermal cells of a human hand. In this experiment, anti-β_1 integrin antibody staining (bright green) showed integrin β_1 distribution in a normal skin (Figure 4A) and in the skin of a healed wound where the papillary dermis had disappeared (Figure 4B). These figures show higher expression of integrin β_1 in epidermal cells closer to the dermal layer (bright zones in A and B) than integrin β_1 expression in distant regions. We also observe that β_1 expression was higher in the normal skin (A) than in the skin of a healed wound (B), suggesting the relation between moderate integrin expression and successful wound healing. These results also implies that integrin β_1 expression in epidermal (keratinocyte) cells may be associated with locations between epidermal keratinocyte cells and dermal fibroblast cells. In the experiment, the specimens from the burnt hand skin of a patient who underwent surgery were fixed in a 0.1 M phosphate-buffered 10% formaldehyde solution for 24 h, dehydrated, and embedded in paraffin (5 μm sections were used). The anti-β_1 integrin antibody dilutions found to be optimal for this study were 1 : 1000. Normal skin was sectioned from the same site of the hand skin of the same patient. We confirm that the experiment of this integrin study was performed in accordance with relevant guidelines and regulations. This study was approved by the Ethical Committee of the Third Military Medical University and the Hospital Clinic Ethics Review Committee of China. Written informed consent was obtained from all participants involved in the study.

These pieces of evidence may indicate the occurrence of paracrine signaling through EGF secreted by fibroblasts which stimulates neighboring keratinocyte's integrin expression. Although there is no data from our previous experiments[37] about specific details of integrins expressed by the keratinocytes, in general, in wound epidermal keratinocytes, the expression of the following integrin heterodimers are up-regulated: $\alpha_3\beta_1$ and $\alpha_6\beta_4$ (laminin-332 receptors), $\alpha_2\beta_1$ (collagen receptor), $\alpha_9\beta_1$, $\alpha_5\beta_1$, $\alpha_v\beta_6$ (receptor for fibronectin, tenascin, and other ligands), and $\alpha_v\beta_5$ (vitronectin receptor), where integrins $\alpha_5\beta_1$ and $\alpha_v\beta_6$ are expressed *de novo*, reviewed in[65].
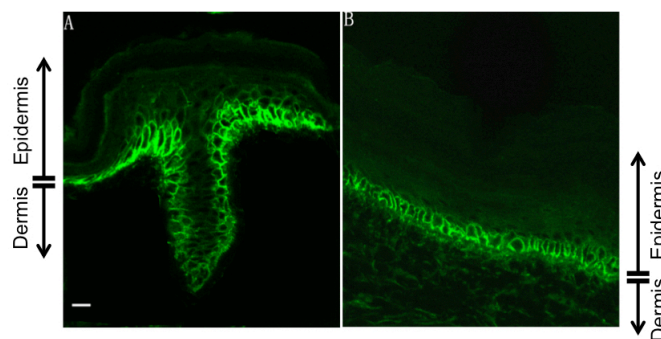

Fig. 4 Immunostaining of β_1-integrin expression. Images taken from normal (A) and after wound healing (B) skins from the same site of a hand of a 26-year old male patient. Scale bar = 10 μm.

2.2 The Model

The Cellular Potts Model (CPM) is a lattice-based modeling technique which was initially used to simulate cell sorting based on differential adhesion. The functionality of the CPM has recently extended to study single cell properties. The model uses an effective-energy formalism to describe the behaviors and interactions of a cell, such as its shape, motility, adhesion with its surroundings (other neighboring cells and/or medium), and also its response to intracellular and extracellular signals[66]. In a Cellular Potts model, a biological cell (termed as a generalized cell) is represented by a collection of pixels (or called voxels for 3D models) having the same index (or cell id) denoted by $\sigma(\mathbf{i})$, where $\mathbf{i}$ denotes the position of a pixel. Cell type for each cell is denoted by $\tau(\sigma(\mathbf{i}))$. In our model, we consider three cell types: fibroblast, keratinocyte, and medium. The medium represents the extracellular matrix (ECM) coated with type I collagen.

2.2.1 The Formulation of Cellular Potts Model for Integrin-mediated Cell Migration

The CPM in this paper is used to study the dynamics of generalized cells by associating an effective energy term with two behaviors: cell adhesion via paracrine signaling and size constraints. The commonly used formulation of the effective energy involving differential adhesion (for the behavior due to cell's interactions with its surroundings) and size constraints is given by the sum of adhesion energy, volume constraint, and surface area constraint, where its Hamiltonian operator is given by[67–69],

$$H = \underbrace{\sum_{\mathbf{i}}^{N}\sum_{\mathbf{j}}^{N} J_{\sigma(\mathbf{i}),\sigma(\mathbf{j})}\left(1-\delta_{\sigma(\mathbf{i}),\sigma(\mathbf{j})}\right)}_{\text{adhesion energy}} + \underbrace{\sum_{\sigma}\lambda_\sigma^{\text{vol}}(v_\sigma - V_t)^2}_{\text{volume constraint}}$$

$$+ \underbrace{\sum_{\sigma}\lambda_\sigma^{\text{surf}}(s_\sigma - S_t)^2}_{\text{surface constraint}}, \qquad (1)$$

where, N, v_σ, s_σ, V_t, S_t, $\lambda_\sigma^{\text{vol}}$, and $\lambda_\sigma^{\text{surf}}$ each denotes the maximal number of generalized cells, volume, area/perimeter, target volume, target area, volume elasticity parameter, and area elas-

ticity parameter, respectively. $J_{\sigma(\mathbf{i}),\sigma(\mathbf{j})}$ is the adhesion energy per unit contact area required to break all adhesive bonds between two generalized cells $\sigma(\mathbf{i})$ and $\sigma(\mathbf{j})$, and $\delta_{\sigma(\mathbf{i}),\sigma(\mathbf{j})}$ is the Kronecker delta function, given by

$$\delta_{\sigma(\mathbf{i}),\sigma(\mathbf{j})} = \begin{cases} 0, & \text{for } \sigma(\mathbf{i}) \neq \sigma(\mathbf{j}) \\ 1, & \text{for } \sigma(\mathbf{i}) = \sigma(\mathbf{j}) \end{cases} \qquad (2)$$

where the factor $(1 - \delta_{\sigma(\mathbf{i}),\sigma(\mathbf{j})})$ ensures that only pixels belonging to different cells that are counted. In the CPM concept, low adhesion energy corresponds to strong adhesion (or attachments) between two generalized cells (or between a cell and medium), whereas high adhesion energy represents weak attachments.

In the skin, keratinocytes and fibroblasts are distributed in separate epidermal and dermal layers, respectively, where they do not mix together. Following this, in our model we assume there is no direct contact between fibroblasts and keratinocytes. Contacts occur between cells of the same type and between a cell and ECM, *i.e.*, between fibroblast-fibroblast, fibroblast-matrix, keratinocyte-keratinocyte, and keratinocyte-matrix. Taking into account these cell-cell and cell-matrix interactions, the adhesion energy term in equation (1) can be expressed in separate cell-cell and cell-matrix adhesion energy terms. Adhesion molecules are considered to be the main determinants of adhesion energy at cell's interfaces, either between cell-cell or cell-matrix[70]. In the formulation, the adhesion energy coefficient $J_{\sigma(\mathbf{i}),\sigma(\mathbf{j})}$ can be replaced by a function containing densities (number/area) of cell surface molecules for cell-cell and cell-matrix adhesion expressed by each fibroblast and keratinocyte on their surface, as well as ligand density in the ECM. Adhesion energy is also regulated by the binding strength between adhesion molecules at contact areas[71,72]. Combining these two factors, the formulation of adhesion energy per unit area between two adhering generalized cells $\sigma(\mathbf{i})$ and $\sigma(\mathbf{j})$ due to adhesion molecule densities and molecule binding affinities is now given by[73],

$$\mathscr{W}_{\sigma(\mathbf{i}),\sigma(\mathbf{j})}^{m,n} = -\sum_{m,n} k_{m,n} \cdot f(N_{\sigma(\mathbf{i})}^m, N_{\sigma(\mathbf{j})}^n), \qquad (3)$$

where, m and n are adhesion molecule labels, $k_{m,n}$ denotes a binding affinity coefficient between a pair of adhesion molecules of different generalized cells, and $N_{\sigma(\mathbf{i})}^m$ and $N_{\sigma(\mathbf{j})}^n$ are adhesion molecule densities of molecule classes m and n expressed on the surface of cells $\sigma(\mathbf{i})$ and $\sigma(\mathbf{j})$, respectively. The non-positivity of this equation is suitable, because, for example, in modeling cell-cell interactions such as cell sorting, increasing the density of adhesion molecules responsible for cell-cell adhesion should minimize cell-cell adhesion energy, provided that the binding affinity coefficient $k_{m,n}$ is positive and cell-matrix adhesion is taken to be constant.

We consider only two binding events regulating the adhesion energy: (i) cell-cell adhesion, which is mediated by E-cadherins N_{σ}^{Ecad} and the binding affinity is denoted by $k_{\text{Ecad,Ecad}}$, and (ii) cell-matrix adhesion, which is due to interactions between integrins N_{σ}^{Int} and ECM ligands N_{σ}^{Coll} whose binding affinity is denoted by $k_{\text{Int,Coll}}$. The function $f(N_{\sigma(\mathbf{i})}^m, N_{\sigma(\mathbf{j})}^n)$ describes binding

dynamics at contact sites between E-cadherin receptors of different cells (cell-cell adhesion) or between integrins and ECM ligands (cell-matrix adhesion). In our model, we assume that each molecule of class m on cell $\sigma(\mathbf{i})$ can bind only once to a molecule n on cell $\sigma(\mathbf{j})$. This relationship is given by the minimum function,

$$f(N_{\sigma(\mathbf{i})}^m, N_{\sigma(\mathbf{j})}^n) = \min\left(N_{\sigma(\mathbf{i})}^m, N_{\sigma(\mathbf{j})}^n\right). \qquad (4)$$

The formulation of adhesion energy in equation (3) appropriately uses a negative sign because, for particularly modeling cell-cell adhesion, the adhesion energy should decrease in order to increase the area of contact between cells. Using this concept in cell-matrix adhesion modeling, low cell-matrix adhesion energy would be equal to an increased probability of cell pixels to attach to the medium/matrix. Increasing cell pixel attachment to the medium by lowering cell-matrix adhesion energy is equivalent to increasing cell motility or migration accompanied by highly irregular morphology. By the formulation in equation (3) above, minimizing cell-matrix adhesion energy (and hence, increased cell motility) could be achieved by increasing the expression of adhesion molecules responsible for cell-matrix interactions, *i.e.*, integrins, provided that $k_{m,n}$ is positive and cell-cell adhesion is taken to be constant. That being said, several experimental studies have indicated the opposite, where, in integrin-mediated cell migration, increasing cell-matrix adhesion (by increasing integrin expression) to the medium should slow down cell migration and lead to immobilization[50,74,75]. In other words, increasing integrin expression should increase cell-matrix adhesion energy because, in the CPM, high cell-matrix adhesion energy leads to cell pixels that dislike the medium, reducing cell motility, and eventually cell immobility. Therefore, to increase cell-matrix adhesion energy via increasing integrin expression, adhesion energy in equation (3) must be positive. In our model, to obtain positive adhesion energy, we take the values of binding affinity coefficient $k_{m,n}$ to be negative. With positive energy, if, for example, the density of molecules N_{σ}^{Int} is increased, adhesion energy $\mathscr{W}$ also increases, leading to weak attachments at the cell periphery that slows cell migration. This concept is vital in our model to capture keratinocyte deceleration causing delayed re-epithelialization and the biology behind it is explained in the next subsection.

Paracrine signaling occurs in the wound healing system, in which, EGF secreted by fibroblasts regulates the expression of integrins, particularly integrin expression of nearby keratinocytes. Hence, integrin expression is modeled to be dependent on EGF concentration $E = E(\mathbf{x})$ where, an increase in EGF concentration leads to an increase in integrin expression. However, the relationship cannot be linear as cells may have maximal integrin expression levels on their surfaces, as observed in experimental studies[76]. Therefore, we apply a saturated function for the relationship between EGF and integrin expression, given by

$$N_{\sigma}^{\text{Int}}(t+1) = \frac{\theta N_{\sigma}^{\text{Int}}(t) + \alpha E^r}{K_1 + \nu E^r}, \qquad (5)$$

where, θ, α, K_1, r, and ν are positive constants. The other molecules, N_{σ}^{Ecad} and N_{σ}^{Coll}, are assumed not to be regulated by

EGF concentration and their expressions are taken to be constants.

The adhesion energy per unit area in equation (3) can be written, after including the two binding events, as

$$\mathscr{W}_{\sigma(\mathbf{i}),\sigma(\mathbf{j})} = -\left(k_{\text{Ecad,Ecad}} \cdot f(N_{\sigma(\mathbf{i})}^{\text{Ecad}}, N_{\sigma(\mathbf{j})}^{\text{Ecad}}) + k_{\text{Int,Coll}} \cdot f(N_{\sigma(\mathbf{i})}^{\text{Int}}, N_{\sigma(\mathbf{j})}^{\text{Coll}}) \right), \tag{6}$$

where,

$$f(N_{\sigma(\mathbf{i})}^{\text{Ecad}}, N_{\sigma(\mathbf{j})}^{\text{Ecad}}) = \min\left(N_{\sigma(\mathbf{i})}^{\text{Ecad}}, N_{\sigma(\mathbf{j})}^{\text{Ecad}} \right), \tag{7}$$

and

$$f(N_{\sigma(\mathbf{i})}^{\text{Int}}, N_{\sigma(\mathbf{j})}^{\text{Coll}}) = \min\left(N_{\sigma(\mathbf{i})}^{\text{Int}}, N_{\sigma(\mathbf{j})}^{\text{Coll}} \right). \tag{8}$$

The net contribution of adhesion to the effective energy is the sum of the adhesion energies at every cell-cell and cell-matrix interface, and is given by

$$\mathscr{W}_{\text{adhesion}} = \sum_{\mathbf{i}}^{N} \sum_{\mathbf{j}}^{N} \mathscr{W}_{\sigma(\mathbf{i}),\sigma(\mathbf{j})} \left(1 - \delta_{\sigma(\mathbf{i}),\sigma(\mathbf{j})} \right). \tag{9}$$

We can see that equation (9) is comparable to the first term on the right hand side of equation (1), hence we can express the CPM effective energy as

$$H = -\sum_{\mathbf{i}}^{N} \sum_{\mathbf{j}}^{N} \left(\underbrace{k_{\text{Ecad,Ecad}} \cdot f(N_{\sigma(\mathbf{i})}^{\text{Ecad}}, N_{\sigma(\mathbf{j})}^{\text{Ecad}})}_{\text{cell-cell adhesion energy}} + \underbrace{k_{\text{Int,Coll}} \cdot f(N_{\sigma(\mathbf{i})}^{\text{Int}}, N_{\sigma(\mathbf{j})}^{\text{Coll}})}_{\text{cell-matrix adhesion energy}} \right)$$
$$\left(1 - \delta_{\sigma(\mathbf{i}),\sigma(\mathbf{j})} \right) + \underbrace{\sum_{\sigma} \lambda_{\sigma}^{\text{vol}}(v_{\sigma} - V_t)^2}_{\text{volume constraint}} + \underbrace{\sum_{\sigma} \lambda_{\sigma}^{\text{surf}}(s_{\sigma} - S_t)^2}_{\text{surface constraint}}, \tag{10}$$

where, $f(N_{\sigma(\mathbf{i})}^{\text{Ecad}}, N_{\sigma(\mathbf{j})}^{\text{Ecad}})$ and $f(N_{\sigma(\mathbf{i})}^{\text{Int}}, N_{\sigma(\mathbf{j})}^{\text{Coll}})$ are given by equations (7) and (8), respectively. In this formulation, the effective energy is now determined by four factors: cell-cell adhesion energy, cell-matrix adhesion energy, volume constraint, and surface constraint.

The evolution of the cellular pattern within the CPM uses Metropolis algorithm to gradually drive down the overall effective energy of the system under study, as formulated in equation (10). The CPM's energy-based formalism is equivalent to the force-based formalisms employed by other cell-based modeling methods. In other words, the results obtained using the CPM or other formalisms should be, at least, qualitatively equivalent provided that the biology/physics implemented in them is the same by assigning probabilities to certain states based on changes in energy over any measure of the system's volatiles. For example, at each step, a pixel **i** is selected at random as a target pixel and one of its neighboring pixel **j** is selected as a source pixel. Then the cell's index is changed from $\sigma(\mathbf{i})$ to $\sigma(\mathbf{j})$ with the following conditions,

$$P_{\sigma(\mathbf{i}) \to \sigma(\mathbf{j})} = \begin{cases} 1 & \text{if } \Delta H < 0 \\ \exp(-\Delta H / T_m) & \text{if } \Delta H \geq 0 \end{cases} \tag{11}$$

where,

$$\Delta H = H_{\text{New}} - H_{\text{Old}}, \tag{12}$$

is the change in the overall system effective energy for each pixel copy attempt. If the change in the effective energy is negative ($\Delta H < 0$), then pixel copy is successful and pixel changes take place. But, if the change in the effective energy is positive ($\Delta H \geq 0$), we accept the change with probability $P = \exp(-\Delta H / T_m)$. The parameter T_m is a constant that determines the flexibility of cell membrane to fluctuate. The amplitude of cell membrane fluctuations is governed by the ratio $\Delta H / T_m$, where high $\Delta H / T_m$ can lead to rigid, less motile cells whereas low $\Delta H / T_m$ exhibits high cell motility. These membrane dynamics are associated with F-actin properties[77].

2.2.2 Relating The Cellular Potts Model to Biology of Cell-matrix Adhesion

Cell migration is a cellular mechanism governed by the interactions between biochemical and mechanical aspects of the components defining adhesion energy, specifically cell-matrix adhesion energy, described in equation (6). These components include integrin expression level, ligand level, and integrin-ligand binding affinity. Integrins in charge of cell migration are concentrated at adhesion structures, which are discrete physical sites on the cell membrane at which the actin cytoskeleton and ECM fibrils converge and are connected via integrins. Particularly for migration on 2D substrates, these adhesion structures are varied in size (protein composition), lifespan, mechanical properties, and subcellular localization[78]. They grow bigger as mechanical tension increases, from ~ 0.25 μm in diameter for 60 seconds to ~ 0.5 μm for 5 minutes, and eventually to a structure bigger than 5 μm[79]. The number of integrin receptors clustered and bound with ligands in each structure also increases as the structure grows bigger[80].

The smallest adhesion structure, referred to as nascent adhesions, are mostly found at the periphery of the leading edge (lamellipodium) of fast moving cells[78,81,82]. Nascent adhesions are thought to be responsible for generating and transmitting strong tractions to push migrating fibroblasts forward, enabling fast migration speed[83]. Nascent adhesions are also linked to rapid migration of Chinese hamster ovary cells[81]. The turnover of nascent adhesions is very high, where they quickly disassemble or grow in size slightly inward along actomyosin bundles into focal complexes and focal adhesions, subsequently. These structures are found around both the lamellipodium and lamellipodium-lamellum interface[78,81]. Some studies observed that cell migration speed on 2D substrates is also optimal at these intermediate adhesion structures[79]. Past a critical adhesion size, the biphasic dependence of cell speed on adhesion renders cell migration speed to decrease as adhesion keeps increasing in size[84]. Growing focal adhesions transform into mature and larger fibrillar adhesions, which are translocated in the lamellum and cell center area[78,85]. While small adhesions are responsible for migration, the largest structure, called fibrillar adhesion, functions to promote ECM remodeling and they are not involved in cell migration[79,86]. Fibrillar adhesions are the most stable adhesion structure, hence they prevent cells from migrating[49,74].

The translocation of these integrin-bound adhesion structures, as illustrated in Figure 5, suggests that cell-matrix adhesion starts

with stronger adhesiveness (consequently, very low adhesion energy) at the cell periphery. When the adhesions grow in size and protein composition, intracellular and extracellular tension causes these structures to move centripetally with stronger adhesion at the cell center area, leaving the cell periphery with weaker adhesion (consequently, higher adhesion energy). This is how the CPM formulation for adhesion energy described in equation (3) is related to the biology of cell-matrix adhesion.
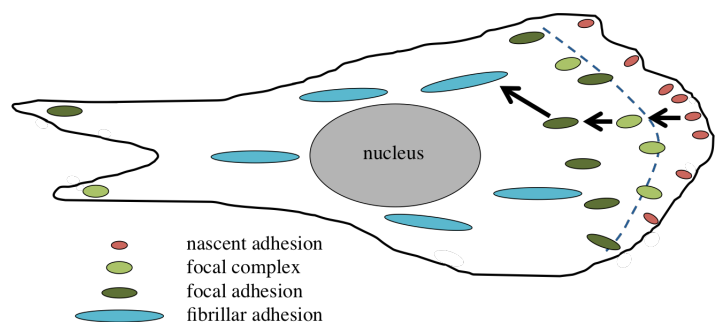

Fig. 5 Illustration of adhesion structure growth and centripetal movement. Schematic illustration of different stages of size and location of adhesion structures that contain different expression levels of integrins. The black arrows show the translocation of adhesion structures from the cell periphery (nascent adhesions) toward the lamellipodium-lamellum boundary (focal complexes and focal adhesions), and eventually the cell center (fibrillar adhesions).

2.2.3 Surface Tension

When integrin expression is varied using equation (5), adhesion energy also changes based on equation (6). The changes in adhesion energy dramatically affect cellular behavior such as cell migration, which can be determined using surface tension. Surface tension is an equilibrium property containing information on tissue cohesiveness[69,87], where, low (or negative) surface tension corresponds to motile individual cells due to very weak cohesion whereas high (and positive) surface tension is related to immobile cells that like to adhere with nearby cells, creating strong cohesion.

In its original formulation intended for modeling of cell sorting patterns, surface tension basically represents the difference in energy between heterotypic and homotypic interfaces per unit area of membrane[68]. For example, if there are two types of cells, *e.g.*, `cell1` and `cell2`, then surface tension equations, that are formulated as

$$\gamma_{\text{cell1,cell2}} = J_{\text{cell1,cell2}} - \frac{J_{\text{cell1,cell1}} + J_{\text{cell2,cell2}}}{2}$$

$$\gamma_{\text{cell1,medium}} = J_{\text{cell1,medium}} - \frac{J_{\text{cell1,cell1}}}{2} \qquad (13)$$

$$\gamma_{\text{cell2,medium}} = J_{\text{cell2,medium}} - \frac{J_{\text{cell2,cell2}}}{2},$$

make it easier for us to approximate parameters for desired patterns. If we want to have a cellular pattern where cells of type `cell1` are encircled by cells of type `cell2`, then we must choose values of J's such that adhesion between cells of type `cell1` and

medium is stronger than adhesion between cells of type `cell2` and medium, or that $\gamma_{\text{cell1,medium}} > \gamma_{\text{cell2,medium}}$ and low $\gamma_{\text{cell1,cell2}}$. In this case, adhesion between cells of type `cell2` and medium must be loose enough because they must move outwardly to provide space for cells of type `cell1` to cohere at the center.

Further formulation using simple dimensional analysis to measure tissue viscoelasticity shows that surface tension is proportional to the multiplication of the number of bound cell adhesion molecules (N) per unit area of a cell and the effective binding energy (k) of a pair of such molecules of two generalized cells, as given by[87],

$$\gamma \propto N k. \qquad (14)$$

This formulation was expanded to calculate surface tension that includes the densities of integrins and E-cadherins and molecule binding affinities[88], which we use for our model in this paper, given by

$$\gamma = \frac{k_{\text{Ecad,Ecad}} \cdot \min(N_{\sigma(\mathbf{i})}^{\text{Ecad}}, N_{\sigma(\mathbf{j})}^{\text{Ecad}})}{2} - k_{\text{Int,Coll}} \cdot \min(N_{\sigma(\mathbf{i})}^{\text{Int}}, N_{\sigma(\mathbf{j})}^{\text{Coll}}). \qquad (15)$$

The surface tension equation (15) above represents the difference in energy between cell-cell and cell-matrix adhesions because of the negative sign used for adhesion energy formulation in equation (3). Negative binding affinity coefficients $k_{\text{Int,Coll}}$ and $k_{\text{Ecad,Ecad}}$ will make equation (15) equal to the formulations in equation (13).

A recent experimental study confirms that an increase in surface tension is related to an increase in tissue cohesiveness or how strong cells adhere to each other[89]. Several studies also showed that integrins are involved in the regulation of surface tension and tissue cohesion[90–92]. The formulation of surface tension in equation (15) can explain the changes in cell migration speed due to varying integrin expressions. Increasing or decreasing integrin expression of the second term on the right side may change the sign and value of surface tension γ. Assuming the molecule binding affinities are all negative, positive surface tension is equivalent to the domination of the term $k_{\text{Int,Coll}} \cdot \min(N_{\sigma(\mathbf{i})}^{\text{Int}}, N_{\sigma(\mathbf{j})}^{\text{Coll}})$ or cell-matrix adhesion energy over the term $k_{\text{Ecad,Ecad}} \cdot \min(N_{\sigma(\mathbf{i})}^{\text{Ecad}}, N_{\sigma(\mathbf{j})}^{\text{Ecad}})$ or cell-cell adhesion energy. Positive surface tension also coincides with weak cell-matrix attachment and strong cell-cell attachment, rendering strong cell cohesion that corresponds to integrin over-expression and generates stable fibrillar adhesions, preventing cells from moving forward. On the other hand, negative (and low) surface tension corresponds to cell-cell adhesion energy which is higher than cell-matrix adhesion energy, causing stronger cell-matrix attachment and leading cells to separate from each other and increase their motility. The combination of integrin dynamics with adhesion strength in our model allows us to explore the interactions of the biochemical and mechanical aspects that govern cell migration.

2.2.4 Model Variables

We discuss the variables of our model in the following parts.

2.2.4.1 Keratinocytes In our model, we assume the following for keratinocytes:

- A fundamental factor that drives keratinocyte migration is cellular adhesion, which is classified into cell-cell adhesion mediated by E-cadherin and cell-matrix adhesion by mediated integrins that binds with collagen of the ECM. In our model, only integrin expression that is assumed to play a role in the wound healing system and to see its effect, the expression is varied over time. E-cadherin expression is taken to be constant and not considered a major factor for cell migration in our model.

- Paracrine signaling occurs in the system, such that, EGF secreted by nearby fibroblasts stimulates the expression of integrin family in keratinocytes that is known to be binding to type I collagen, as is modeled in equation (5).

- High concentration of EGF influences cell-matrix adhesion through integrin-ligand affinities, leading to cell speed deceleration. This is observed in experiments as shown in Figure 3.

- EGF also reduces the strength of keratinocyte's cell-matrix adhesion at all ECM ligand concentrations [57,93,94].

- Since our topic is on integrin-mediated migration, the level of E-cadherin and collagen densities are assumed not to be affected by EGF concentration and taken to be constant.

- Keratinocytes are considered motile cells with migration speed ranging between 0.86 to 1.11 mm/day [37] and have higher rate of membrane fluctuation than fibroblasts.

- Keratinocyte proliferation is not included as our focus is on cell migration aspects.

2.2.4.2 Fibroblasts Our assumptions for fibroblasts are as follows:

- Similar to keratinocytes, the dominating factors that drive fibroblast migration are cell-cell adhesion mediated by E-cadherin and cell-matrix adhesion mediated by integrin binding with collagen.

- Fibroblasts are considered slow moving cells, with typical speed as low as 0.115 mm/day [95]. We assume only EGF secreted by fibroblasts that plays role in our keratinocyte-fibroblast wound healing system, hence fibroblasts solely act as EGF producer and make no or very slow movement.

- Because of its slow movement, fibroblast membrane fluctuation is assumed to be much smaller than that of keratinocytes.

- The migration of fibroblasts is neglected because their migratory behavior did not affect monoculture or co-culture with keratinocytes in our experimental results [37], either in the absence or presence of mechanical stretch.

- Fibroblasts secrete EGF that affects keratinocytes in a paracrine signaling manner.

- Fibroblasts are not affected by their own EGF secretion nor by EGF secreted by keratinocytes.

- Fibroblast proliferation is not included in the model.

2.2.4.3 Epidermal Growth Factor (EGF) EGF or epidermal growth factor is secreted by both keratinocytes and fibroblasts. For monoculture keratinocytes, the stimulation of EGF secretion by mechanical stretch influences their own migration in which they migrate faster with EGF stimulation than without, whereas monoculture fibroblasts are not affected by EGF. In co-culture cases, both fibroblast and keratinocyte cells secrete EGF. However, EGF secreted by keratinocytes is assumed to be much less than EGF secreted by fibroblasts, hence it can be neglected. In our model, the EGF secreted by fibroblasts influence keratinocytes in two ways: (i) increasing keratinocyte's integrin expression and (ii) reducing keratinocyte's integrin-ligand binding affinity. These two then lead to the deceleration of keratinocyte migration speed. We assume that the rate of change of EGF concentration over time is governed by diffusion, secretion by fibroblasts and keratinocytes, and EGF natural decay, given by

$$
\frac{\partial E(\mathbf{x})}{\partial t} = D_E \nabla^2 E(\mathbf{x}) + \phi \delta \left(\tau(\sigma(\mathbf{x})), F \right) + \beta \delta \left(\tau(\sigma(\mathbf{x})), K \right)
$$
$$
- \eta E(\mathbf{x}) \delta \left(\tau(\sigma(\mathbf{x})), M \right), \tag{16}
$$

where

$$\delta \left(\tau(\sigma(\mathbf{x})), F \right) = 1 \text{ inside fibroblast cells } F \text{ and 0 elsewhere,}$$

$$\delta \left(\tau(\sigma(\mathbf{x})), K \right) = 1 \text{ inside keratinocyte cells } K \text{ and 0 elsewhere,}$$

$$\delta \left(\tau(\sigma(\mathbf{x})), M \right) = 1 \text{ inside medium } M \text{ and 0 elsewhere,}$$

D_E, ϕ, β, and η are positive constants that determine EGF diffusion coefficient, rate of EGF secretion by fibroblasts, rate of EGF secretion by keratinocytes, and rate of EGF decay, respectively. Since the effects of EGF secreted by keratinocytes can be neglected, in co-culture cases the constant β is taken to be zero.

2.2.4.4 Collagen Collagen is one of the main components of extracellular matrix. In our model, we assume type I collagen makes up the extracellular environment for both keratinocytes and fibroblasts. We do not explicitly model collagen and it is assumed to be a homogeneous medium with constant density everywhere in the domain.

3 Simulation Results

We implemented the formulation of our Cellular Potts model described in the Materials and Methods section using CompuCell3D (or CC3D for short), which is an agent-based modeling framework for simulating Cellular Potts models. The modeling framework was developed by the Biocomplexity Institute at Indiana University, USA. In this section we present the results of computational simulations, and, the first part of the results uses the default parameter values listed in Table 1 and in the second part, where we present model validation, we altered some parameter values. The altered parameter values are given in the Fitting The Simulation Results To Experimental Data subsection. The CC3D

code to simulate the co-culture model can be found in the Supplementary Information.

3.1 Parameter Approximation

Because keratinocytes in wound healing re-epithelialization migrate laterally, we performed only 2D computational simulations. In our previous experimental work[37], a rectangular tensile device of size 42×20 mm (length $\times$ width) was used for both mono-culture and co-culture conditions. In monoculture experiments, either keratinocytes or fibroblasts were seeded in the center area of the tensile device with an initial width about 8 mm. In co-culture experiments, fibroblasts (1×10^5 cells/cm^2) were seeded with less cell density than keratinocytes (5×10^5 cells/cm^2) and an 11.4 mm initial gap was arranged between keratinocyte and fibroblast sheets. Simulations with 10^5 cells for our semi-multiple scale model (where, cellular scale is combined with intracellular and extracellular dynamics) are computationally expensive. Hence, we limited the number of our cells to the order of 1×10^3 cells, which was sufficient to generate simulations with decent running times. Due to the stochastic nature of the CPM, where each result can give slight variations, we performed 5 simulations for each parameter set and presented the mean values.

Taking 1 pixel equals 0.1 mm, all simulations employed a square lattice. A 300×200 pixels domain was used for mono-culture simulations for both keratinocytes and fibroblasts, where cells were initially distributed in the center of the domain forming like a rectangular sheet, positioned between pixel points 110 and 190 in the x-direction (sheet length equals 80 pixels) and between pixel points 10 and 190 in the y-direction (sheet width equals 180 pixels).

Co-culture simulations used a bigger domain of size 450×200 pixels. Initially, keratinocyte sheet was arranged to have an 80 pixel length (positioned between pixel points 110 and 190 in the x-direction), whereas the initial length of fibroblast sheet was 60 pixels or arranged between pixel points 325 and 385 in the x-direction, representing a lesser fibroblast density as in experiments. Both cell sheets had the same width, 180 pixels in the y-direction. The initial length (or diameter) of a single cell (applied to both keratinocytes and fibroblasts) was taken to be 3 pixels, hence the initial volume of a 2D cell is 9 pixels. This arrange-ment generated 1620 cells for keratinocytes and 1200 cells for fibroblasts. Fibroblasts are a less motile cell than keratinocytes. It is suitable to assign a smaller fibroblast's membrane fluctuation $T_{m,f}$ than keratinocyte's $T_{m,k}$. The amplitudes were taken to be $T_{m,f} = 7$ and $T_{m,k} = 80$. This high fluctuation of keratinocytes is needed to ensure cell motility due to F-actin properties[96]. Be-cause of high membrane fluctuation, if cell's target volume is small (*e.g.*, 10 pixels), cells will be easily fragmented and without strong resistance to volume fluctuation ($\lambda_\sigma^{\text{vol}}$), pixels are quickly diminished/depleted. Therefore, cell's target volume was taken to be higher than the actual cell size, that is $V_t = 20$ with volume constraint $\lambda_\sigma^{\text{vol}} = 25.0$.

For 2D simulations, the nomenclature "cell volume" refers to the number of pixels that cover the area of a cell, whereas "cell surface" is the perimeter or the number of pixel points around cell's outer boundary (it is the number of outer surfaces of vortices for 3D simulations). Because of the small size of our cells, the appropriate choice for the order of neighbor pixels was taken between 2 and 3. To ensure membrane flexibility, we applied the ratio $V_t/S_t = 1$ to determine the target surface area. If the ratio is much bigger than one, cell's inclination to minimize its surface area relative to its volume will generate less flexible and close to rigid membrane. Therefore, the target surface area was also taken to be $S_t = 20$ with surface constraint $\lambda_\sigma^{\text{surf}} = 15.0$.

Since fibroblast migration was neglected, they were assumed to have constant integrin and E-cadherin densities, which were taken to be 4 molecules/area. Keratinocyte's E-cadherin density was also taken to be constant, 4 molecules/area. The only molecule density that changed during simulations was keratinocyte's integrins, whose minimum and maximum were taken 4 and 15 molecules/area, respectively. The medium that contains collagen was assumed to have density 15 molecules per area that is in contact with cells. How adhesion energy and adhesion strength affect cell speed can be examined by varying two key components in our model, which are integrin density N_σ^{Int} and integrin-ligand binding affinity constant $k_{\text{Int,Coll}}$. We varied the values of integrin-ligand binding affinity constant $k_{\text{Int,Coll}}$ manually whereas integrin density variation due to EGF concentration was implemented by applying the formula in equation (5). Throughout the paper, the values of $k_{\text{Int,Coll}}$ were taken to be -1.5, -2.0, -2.5, and -3.0 for co-cultures of keratinocytes and fibroblasts and -1.0, -2.0, -3.0, and -4.0 for monoculture simulations.

Keratinocyte migration in the re-epithelialization phase usually takes place collectively, or in the form of epithelial (sheet) migration where cells adhere to each other through cell-cell adhesion. This form of migration usually requires the existence of leader cells to guide other cells to migrate so that directed migration is achieved effectively[97]. In the CPM, without applying strong external force, collective epithelial migration is difficult to achieve. Since we do not apply external force and keratinocyte migration in our model is only relied on cell-matrix interactions (with the help of high membrane fluctuation), keratinocytes everywhere (those at the front or within the group) moved randomly. Factors such as domain shape, initial cell layout, and cell density helped keratinocytes migrate to the right and left of the rectangular domain. To resemble cell migration in the re-epithelialization phase, keratinocytes in our model must detach from the main sheet so that adjacent individual cells move together prompting collective-like migration. For this purpose, $k_{\text{Ecad,Ecad}}$ was taken to be a lot smaller than $k_{\text{Int,Coll}}$, and in this paper $k_{\text{Ecad,Ecad}} = -13.0$.

To get a reference value for the speed of migrating keratinocytes, we referred to the speed of the fastest moving cells, which are co-culture keratinocytes with EGF stimulation. It is necessary to take the highest speed as a reference because we wanted to track solely keratinocyte migration without being surrounded by fibroblasts, and thus the right-moving keratinocytes (toward fibroblasts) must not be mixed with fibroblasts. Therefore, keratinocytes must reach their longest displacement distance on day 6 or right before they coalesce with (or touch) fibroblasts. This is the same time reference set in experiments. From Figure 3

(data case 4), we deduce that the average speed is slightly above 1 mm/day, or 10 pixels/day, and within 6 days keratinocytes have been displaced ~ 6.7 m due to deceleration. To measure cell displacement, we tracked the centroid (or positions in the x- and y-directions) of keratinocytes that move to the right (toward fibroblasts) and to the left (away from fibroblasts). The reference point $(0,0)$ is located at the bottom left of the domain. We can then adjust some parameters to obtain displacement distance with quantities close to experimental data.

The duration of simulations was measured in Monte Carlo Steps (MCS) and to get the intended speeds and displacement distances, in all simulations 1 MCS was scaled to 2 minutes. Using this time scale, we estimated 1 day ~ 700 MCS. Because each cell was initialized having a square shape (with initial size 3×3 pixels^2) and over time the target volume was constrained to 20 pixels, we let the cells grow and take a spherical shape by letting the simulations run up to 200 MCS before starting implementing the intracellular and extracellular dynamics formulated in equations (5) and (16). Hence, day 1 was measured at 900 MCS, day 2 at 1600 MCS, and so on until day 6 at 4400 MCS. With this choice of time scale, combined with other parameters mentioned above, significant intended migration patterns will be observed around the same days as experiments in [37].

The EGF diffusion constant D_E was taken to be 0.25 pixel^2/MCS. With scaling 1 pixel^2 = 0.01 mm^2 and 1 MCS = 2 mins, the choice of 0.25 pixel^2/MCS is equal to 2.083×10^{-7} cm^2/s, which is close to the order of diffusion constant suggested in [98]. The EGF decay rate was taken to be ~ 0.0024 MCS^{-1} or $\eta \sim 2 \times 10^{-5}$ s^{-1}. For coculture simulations, we assume only EGF secreted by fibroblasts that has a significant role in keratinocyte migration, hence we took $\beta = 0$ in equation (16). For the rate of EGF secreted by fibroblasts, we took $\phi = 0.2$ nM pixel^{-1} MCS^{-1}. The initial and boundary conditions of EGF were 0 and zero-flux, respectively.

3.2 Parameter Analysis

In this subsection we investigate analytically what kind of results we shall obtain from our model using the parameters listed in Table 1 and to make *a priori* predictions if the parameters are varied.

To obtain positive adhesion energies in equation (3), we take the binding affinity constants $k_{\text{Ecad,Ecad}}$ and $k_{\text{Int,Coll}}$ to be negative. It is also preferable to deal with positive adhesion energies in modeling integrin-mediated cell migration, because, negative energies can cause cells to disintegrate, especially if we exclude surface area constraint (or, if we only use volume constraint). The use of positive/negative adhesion energy in the CPM has been discussed in some studies [69]. Initially, with $N_\sigma^{\text{Int}} = 4$, $k_{\text{Int,Coll}} = -1.0$, $N_\sigma^{\text{Ecad}} = 4$, and $k_{\text{Ecad,Ecad}} = -13.0$, cell-matrix adhesion energy will be much lower than cell-cell adhesion energy. Low cell-matrix adhesion energy (corresponds to strong cell-matrix attachment/adhesivity) and high cell-cell adhesion energy (weak cell-cell attachment/adhesivity) will prompt cells to migrate with high propensity and separate from each other. Low cell-matrix adhesion energy stimulates cells to migrate faster in the first few days,

particularly on days 1 and 2, which can be related to the movement of cells driven by small adhesion structures such as nascent adhesions, focal complexes, and/or focal adhesions. Because of the biphasic behavior, as the size of adhesions is getting bigger and after a critical adhesion size has been reached, growing adhesions (that translocate to the cell center) now promote slower migration speed and eventually halt cell movement. We simulated this by increasing integrin expression using equation (5), by which cell-matrix adhesion energy also becomes higher, resulting in weaker cell-matrix attachment at the cell perimeter. We assume that the critical adhesion size is obtained some time between day 1 and day 2, with a critical integrin density between $N_\sigma^{\text{Int}} = 6$ and $N_\sigma^{\text{Int}} = 7$. Past this value, cell speed starts to decelerate as integrin density keeps increasing. Our model makes use of increasing cell-matrix adhesion energy to simulate subsequent acceleration and deceleration keratinocytes, causing inevitable delayed re-epithelialization. The linear relationship between energy and ligand-bound integrins, *i.e.*, the number of integrin bindings with ligand increases as energy also increases, has been shown in another theoretical study [71]. Varying integrin-ligand binding affinity $k_{\text{Int,Coll}}$ can also influence cell migration. For example, with integrin density $N_\sigma^{\text{Int}} = 4$, if integrin-ligand binding is taken to be low, which is $k_{\text{Int,Coll}} = -2.0$ or $k_{\text{Int,Coll}} = -3.0$, it will weaken the binding strength between integrins (cell) and ligands (matrix) at the cell perimeter. By the formulation in equation (6), lowering $k_{\text{Int,Coll}}$ amounts to increasing cell-matrix adhesion energy, and consequently, slowing cell migration [49].

Our model revolves around varying/increasing integrin expression and integrin-ligand binding affinity via the function f $(N_{\sigma(\mathbf{i})}^{\text{Int}}, N_{\sigma(\mathbf{j})}^{\text{Coll}})$, which ensures that there is a maximal binding number between integrins and ligands. If integrin density keeps increasing and at some point becomes higher than ligand density, the value of ligand density (which is constant) will be automatically assigned to be the binding number as the simulation progresses. Hence, $f(N_{\sigma(\mathbf{i})}^{\text{Int}}, N_{\sigma(\mathbf{j})}^{\text{Coll}})$ will be constant if integrin density is higher than ligand density. We limit the upper number of integrin density to 15 molecules/area, which is similar to ligand density constant. The relatively small values of molecule densities along with binding affinity constants allow us to observe the effects of negative and positive surface tensions, equally. In the CPM, it is allowed to use wider ranges of molecule density expression, as long as surface tensions are not too high or too low, hence, high integrin or cadherin expressions must be balanced with low binding affinity constants. With the parameters used in our model (*e.g.*, $\lambda_\sigma^{\text{surf}}$, S_t, etc.), the values of surface tension should be between $-20 < \gamma < 20$. Surface tension values beyond these limits can create cell-lattice-alignment artifacts. In our CC3D code, integrin density expression in equation (5) is implemented deterministically (without random changes).

We now look at the role of surface tension and integrin density along with integrin-ligand binding affinity in guiding cell speed. If we apply constant values for $k_{\text{Int,Coll}}$, $k_{\text{Ecad,Ecad}}$, and N_σ^{Ecad}, increasing integrin density leads to increased surface tension. Using the parameters in Table 1 and $k_{\text{Int,Coll}} = -1.5$, surface tension starts at $\gamma = -20$. If N_σ^{Int} is increased from 4 to 15, γ also increases but never reaches zero. This is shown by the blue line of plots

of integrin expression vs surface tension in Figure 10. In the region of $\gamma \ll 0$, cell motility is high, tissue cohesion is very low, and individual cells move fast. As γ approaches zero, cell speed starts to decrease but migration is still maintained. Surface tension may reach positive value if the range of integrin expression is extended beyond 15 and at the same time increasing ligand density N^{Coll} higher than 15 as well. Decreasing binding affin-ity to $k_{Int,Coll} = -2.0$ amounts to higher surface tension, where now surface tension has positive and negative regions as N^{Int} is increased from 4 to 15 and the boundary of the regions ($\gamma = 0$) is achieved at around $N_{\sigma}^{Int} \approx 13$. Above $\gamma = 0$, if surface tension continues to increase, cells migration decelerates. Cells will cease to migrate if surface tension keeps going higher. Positive surface tension causes cell cohesion, where adjacent cells become adhere to each other. If integrin-ligand binding affinity is reduced further, now with $k_{Int,Coll} = -2.5$ or $k_{Int,Coll} = -3.0$, the region boundaries, where $\gamma = 0$, shift to lower values of N_{σ}^{Int}. Deceleration and cell cohesion then occur at lower integrin densities.

Altering energies by modifying adhesion components and size constraints as explained above enables us to control cell motility individually. To manage cell global speed in the system, we use the parameter T_m. The rigidity of keratinocytes and fibroblasts is predicted using the ratio $\Delta H/T_{m,k}$ and $\Delta H/T_{m,f}$, respectively. It is of interest to be able to control cell's membrane fluctuation, especially our model has two cell types where each has different migration speeds. For example, if ΔH is equal 100 (and this value does not necessarily represent the actual ΔH calculated from our model), with $T_{m,f} = 7$, the ratio of fibroblast's membrane fluctuation $\Delta H/T_{m,f}$ is one order higher than keratinocyte's $\Delta H/T_{m,k}$ with $T_{m,k} = 80$. The difference in the magnitudes of membrane fluctuation gives significantly different results, as we will observe in the following subsections.

3.3 Monoculture Simulations

The results of monoculture simulations with constant integrin expression are presented in Figs. 6 (for keratinocytes) and 7 (for fibroblasts). In these figures, the expressions of all adhesion molecules are taken to be constant, where $N_{\sigma}^{Int} = N_{\sigma}^{Ecad} = 4$, and $N_{\sigma}^{Coll} = 15$. Figure 6 shows the comparison of migrating distances between monoculture keratinocytes that have high membrane fluctuation $T_{m,k} = 80$ with different values of integrin-ligand binding affinity coefficient $k_{Int,Coll}$. Each column represents results on day 1 (left column), day 3 (middle column), and day 6 (right column) while each row represents results with $k_{Int,Coll} = -1.0$ (top row), $k_{Int,Coll} = -2.0$ (second row from top), $k_{Int,Coll} = -3.0$ (third row from top), and $k_{Int,Coll} = -4.0$ (bottom row).

Using the same parameter values in the simulations for keratinocytes, except that the membrane fluctuation coefficient is now set to $T_{m,f} = 7$, the results of simulations for fibroblast cells with the highest $k_{Int,Coll}$ are shown in the top figures of Figure 7 and the lowest $k_{Int,Coll}$ are shown in the bottom figures. To quantify the migration of keratinocytes and fibroblasts in monoculture simulations, we tracked positions of one cell, located in the middle of the edge of keratinocyte/fibroblast sheets, every day for each value of $k_{Int,Coll}$ and the results are shown in Figure 8.

For keratinocyte monocultures, we can observe that the relation between integrin-ligand binding affinity and cell motility is linear, that is increasing integrin-ligand binding affinity coefficient stimulates cell migration speed, as shown in Figure 8(a). From these monoculture simulations of keratinocytes and fibroblasts, twofold key points we can take are: first, with a constant inte-grin expression, cell migration speed can be controlled by varying integrin-ligand binding affinity. Second, if the ratio of membrane fluctuation $\Delta H/T_m$ is high, varying integrin-ligand binding affinity has little effects on cell speed as shown in Figure 8(b), in which cells are rigid and remain less motile until the end of simulation. On the other hand, low membrane fluctuation ratio contributes to high speed when varying integrin-ligand binding affinity, as shown in Figure 6.

We now investigate how varying integrin expression and integrin-ligand binding affinity affects cell migration and the simulation results are presented in Figure 9. In these results, the initial density of integrins is $N_{\sigma}^{Int} = 0.1$ and using the following function,

$$N_{\sigma}^{Int}(t+1) = \omega + N_{\sigma}^{Int}(t), \qquad (17)$$

where, $\omega = 0.01$, integrin expression of all cells is linearly increased. Other molecule densities are taken to be constant, $N_{\sigma}^{Ecad} = 4$ and $N_{\sigma}^{Coll} = 15$, and other parameters are taken as in Table 1 with membrane fluctuation $T_m = 80$, which is basically parameters for monoculture keratinocytes in Figure 6.

Comparing the results in Figure 9 with those in Figure 6, we observe that by varying integrin expression and integrin-ligand binding affinity, the effects of increased energy and surface tension are now visible. At the highest integrin-ligand binding affini-tiy $k_{Int,Coll} = -1.0$, cells move with normally high speed up to day 3. But when integrin expression is higher, as seen on day 6, cell speed starts to slow down, compared to cells on day 6 in Figure 6. Reducing integrin-ligand binding affinity to $k_{Int,Coll} = -1.5$ leads to increased cell-matrix adhesion energy and weaker cell-matrix attachment strength at the cell periphery, decreasing cell migration speed, as shown by figures in the middle row of Figure 9. At even lower binding affinity, with $k_{Int,Coll} = -2.0$, cells are suppressed from moving forward and they tend to bind/adhere with their neighboring cells, forming what it seems like tissue cohesion, as shown by figures in the bottom row of Figure 9. Tissue cohesion is related to surface tension, as has been explained previously in the Materials and Methods section.

Implementing the variation of integrin expression for each $k_{Int,Coll}$ in equation (15) for surface tension produces different surface tension regions as integrin expression increases. At $k_{Int,Coll} = -1.5$, the values of surface tension is always negative although increasing toward zero. This is caused by the minimum function in the surface tension equation, which ensures only integrin expression within the range of $[0.1, 15]$ shall be used in the surface tension equation. When integrin-ligand binding affinity is reduced to $k_{Int,Coll} = -2.0$, surface tension now has positive and negative regions where $\gamma = 0$ (the start of cell cohesion) takes place around day 2, as shown by figures in the bottom row of Figure 9. Cohesiveness due to increasing integrin expression is important to capture delayed re-epithelialization, in which ker-

atinocytes fail to move forward to cover wound sites at which integrin expression is very high[33], giving rise to chronic wounds.
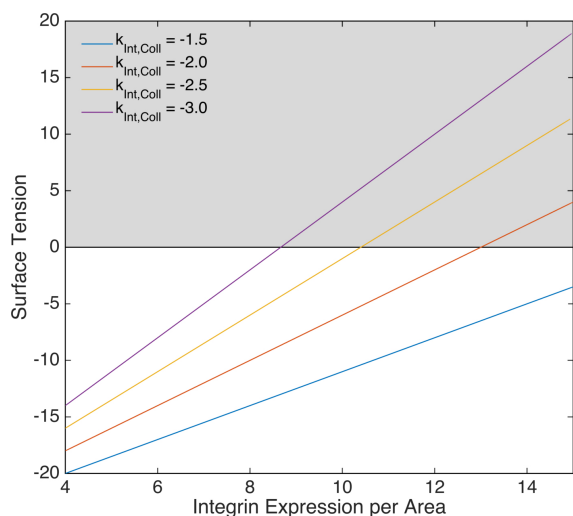

Fig. 10 Predicted variations of surface tension as integrin expression is increased. Plots are generated using equation (15) and parameters in Table 1 with different values of integrin-ligand binding affinity $k_{\text{Int,Coll}}$. Cells whose surface tension is negative (white region) are inclined to be motile and migrate faster as surface tension decreases, whereas positive surface tension (grey region) causes cells to decelerate and restrain from migrating forward if surface tension increases.

The variation of surface tension against integrin expression is shown in Figure 10, where cells having high integrin-ligand binding affinity, $k_{\text{Int,Coll}} = -1.5$ maintain their high motility because their surface tension values remain negative (blue line). On the other hand, cells with lower affinities embrace two surface tension regions: cells are motile when their surface tension is negative and as surface tension becomes positive their speed decelerates and the cells eventually stop moving forward as their surface tension goes higher. These plots are valid for simulations using parameters in Table 1. If the levels of maximal expression of integrins and ligands are increased, thus changing the minimal binding number in $f\left(N_{\sigma(\mathbf{i})}^{\text{Int}}, N_{\sigma(\mathbf{j})}^{\text{Coll}}\right)$, cells with high $k_{\text{Int,Coll}}$ will in the long run have negative and positive surface tension regions as well. These results confirm that cell migration speed depends on the dynamics of integrin binding with ECM ligands, in our model represented by equation (4), which, is dependent on integrin and ligand densities, as well as their binding strength.

Aside from surface tension, another way to parameterize the effect of varying integrin expression on cell motility is by using two physical quantities of a cell resulted from simulations, *i.e.*, cell volume and surface. These quantities determine cellular shape or morphology, commonly named circularity and given by

$$\text{circularity} = \frac{4\pi\,\text{volume}}{\text{surface}^2}. \tag{18}$$

By the above equation, if the value of circularity is close to 1.0, it indicates a cell shape that approaches a perfect circle. And if the value approaches 0, the cell is increasingly elongated.

Circularity has been used as a measure of cell morphology that is linked to cell motility, where the elongation of a cell body cor-

relates with cell's motile behavior[99]. We use this measure to assess if varying integrin expression and the choice of positive or negative integrin-ligand binding affinity influence cell motility. Curve fittings of the results using linear regression are shown in Figure 11. In figures 11(a) and 11(b), integrin expression is increased indefinitely from $N_{\sigma}^{\text{Int}} = 0.1$ based on equation (17) until simulations end at $10,000$ MCS. We observe that the plot for negative integrin-ligand binding affinity $k_{\text{Int,Coll}}$ is inclined, denoting increased circularity from around ~ 0.5 to ~ 0.6. It signifies that over time cell shape becomes more regular, although never close to a circle. It is important to note that if we use a square lattice, we will not be able to get a perfect circle. The closest shape to a circle is a square, where its highest value of circularity is ~ 0.78. As opposed to negative $k_{\text{Int,Coll}}$, using positive $k_{\text{Int,Coll}}$ reduces circularity from ~ 0.5 to around ~ 0.2. In this case, cell-matrix adhesion energy decreases and the cell becomes very motile with irregular and elongated shapes. If circularity is very low (approaches zero), it indicates that cell surface has become very much larger than cell volume and cell body can disintegrate into individual pixels.

To examine whether the variation in circularity is in fact a result of varying integrin expression, we also ran two simulations with constant integrin expression, $N_{\sigma}^{\text{Int}} = 0.1$ as shown in figure 11(c) and $N_{\sigma}^{\text{Int}} = 50$ as in figure 11(d), both using negative integrin-ligand binding affinity $k_{\text{Int,Coll}} = -1.0$. From these simulations, it is confirmed that with low integrin expression, which corresponds to low cell-matrix adhesion energy (at the cell periphery), cell motility is high as signified by low circularity. And with high integrin expression, which means high cell-matrix adhesion energy, circularity is high, indicating low cell motility. Other parameters used in these simulations, such as V_t, S_t, $\lambda_{\sigma}^{\text{vol}}$, and $\lambda_{\sigma}^{\text{surf}}$, are as in Table 1, with $T_m = 80$. To let integrin expression increased indefinitely without being affected by the minimum function in equation (4), we set $N_{\sigma}^{\text{Coll}} = 500$.

3.4 Co-culture Simulations

To study the effects of paracrine signaling of EGF secreted by fibroblasts on keratinocyte migration, in co-culture simulations keratinocyte and fibroblast sheets were placed opposite each other on a rectangular domain that is coated with type I collagen. Following our previous experiments[37], throughout the simulations keratinocytes were placed on the left and fibroblasts on the right side of the domain. We assume that keratinocytes outnumber fibroblasts and both cell types do not undergo mitosis/proliferation[37]. The setup of co-culture simulations is shown in Figure 12(A). Over time, EGF secreted by fibroblasts diffuses in all directions and its gradient is eventually perceived by nearby keratinocytes. The gradient field of EGF from fibroblasts diffusing across the domain is shown in Figure 12(B).

Without going into detail on intracellular pathways of EGF and integrins, we assume that EGF secreted by fibroblasts regulates the expression of integrin receptors on keratinocyte surfaces via equation (5), as well as integrin-ligand binding affinity $k_{\text{Int,Coll}}$ which is also an essential variable in the formulation of adhesion energy, and in controlling cell migration speed. In some simula-
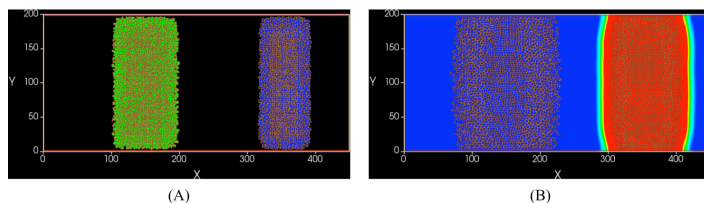
Fig. 12 Initial setup for co-culture simulations. Figure (A) on the left shows a setup for co-culture simulations which follow experiments in[37]. In a rectangular domain, keratinocytes are placed on the left side and separated from fibroblasts. Figure (B) shows EGF field propagation that is secreted by fibroblasts on the right.

tions, the values of $k_{Int,Coll}$ were fixed for each simulation. There are also simulations where the binding affinity of integrins with their ligands was controlled by EGF, as has been observed experimentally[100,101]. Examples of simulation results with $D_E = 0.25$ and $\phi = 0.2$ are shown in Figure 13, where the left column shows screenshots of the spread of keratinocytes with $k_{Int,Coll} = -1.5$, and the right column with $k_{Int,Coll} = -2.0$, both are taken on day 1 (top row), day 3 (middle row), and day 6 (bottom row). At initial times, cells that are initially arranged without gap between each other become separated from each other because of the medium filling up the space between cells, due to strong cell-matrix attachment (or low cell-matrix adhesion energy). At this stage, surface tension is negative and very low. Migrating keratinocytes start to move toward less crowded (or empty) spaces near them while fibroblasts tend to be stationary or make very little movement. Up to day 3, keratinocytes seem to move freely to the right and left sides. On day 6, the difference in cell speed is more observable for lower integrin-ligand binding affinity $k_{Int,Coll} = -2.0$, where keratinocytes moving to the right (toward fibroblasts) exhibit cell cohesion indicating restrained movement. This indicates that keratinocytes moving to the right have expressed very high integrin receptors causing positive and high surface tension. Although there is no direct contact between keratinocytes and fibroblasts, should there be contacts between these cell types, their interactions are defined by cell-cell adhesion (which is constant) and weak attachment (high adhesion energy) causing cells to repel each other.

Like in monoculture simulations, we also tracked positions of keratinocytes in co-culture simulations as they moved along in the x-axis direction, shown in Figure 14. Because cells were initially arranged in a rectangular sheet, as they grew from MCS= 0 they tended to form aggregates with a convex-like shape. Therefore, we only tracked two keratinocytes located in the middle of the right and left edges of the sheet, assuming that the distances of these two cells as they are migrating represent the maximal displacement. One keratinocyte cell located at the center of the right edge of keratinocyte sheet, identified as `Cell ID` 810 in our CC3D code, moved to the right side of the domain or toward the fibroblasts, while the other cell located in the middle of the left edge of the keratinocyte sheet, identified as `Cell ID` 811, moved to the left or away from fibroblasts. We ran five simulations for each parameter variation and presented the quantifying positions

with mean ± standard deviation.

In Figure 14, the top row figures show average cumulative distances of keratinocyte moving to the left (blue line) and to the right (yellow line), while simulation screenshots represent-ing cells and EGF field on day 6 are presented in the bottom row figures. As our model and parameters predict, cells with $k_{Int,Coll} = -1.5$ only have negative surface tension, thus all ker-atinocytes moving either to the right or left are highly motile. However, keratinocytes moving to the right are exposed to high EGF concentration that quickly elevates their integrin expres-sion, causing keratinocytes to reduce their migration speed. Here keratinocytes still maintain their motility and cell cohesion has not occurred. If we reduce integrin-ligand binding affinity to $k_{Int,Coll} = -2.0$, the average cumulative distance of keratinocyte moving to the right exhibits a saturation growth rate-like curve. It indicates that the tracked cell has entered the positive surface tension region where it undergoes deceleration followed by re-strained migration, and the cell eventually attaches with neigh-boring cells, as can be seen in the bottom right figure. For each simulation result, the surface tension variation of keratinocyte moving to the right is shown in each insert figure, whereas integrin expression of keratinocyte moving to the left remains constant (at its initial value $N_\sigma^{Int} = 4$) and therefore, its surface tension is also constant and always negative (not shown here).

From the top figures of Figure 14, we observe that in the first two days the cumulative migration distances are higher than the rest days, for both keratinocytes moving to the right (represented by yellow line) and left (blue line). It indicates that the tracked cells move rapidly while their integrin expressions are still low, equivalent to cells moving mediated by small adhesions, such as nascent adhesions, focal complexes, or focal adhesions. It is important to note that in our model we do not specify adhesion structure sizes and their integrin expression levels. And as has been explained in the Parameter Analysis section, the critical adhesion size at which cell migration is maximal is assumed to be occurring between day 1 and day 2. From the plots of cumulative migration distances observed each day, the tracked keratinocyte moving to the right with $k_{Int,Coll} = -2.0$ experiences the biphasic dependence of cell speed on integrin expression due to EGF secreted by fibroblasts, where its speed accelerates from day 0 and starts to decelerate after day 2. The deceleration and eventually restrained migration promotes delayed re-epithelialization which can lead to obstructions in the wound healing process. Cell migration influenced by a biphasic behavior due to EGF concentration has been observed previously in several experimental studies using epidermal keratinocytes[14,16,33,36]. In depth studies of the biphasic dependence of cell speed on ligand density and integrin-ligand binding have been carried out[51,59,60,102] and in this paper we focus on integrin density. Using the integrin expression formulation in equation (5), we want to make sure that

$$\frac{\alpha E + \theta N_\sigma^{Int}}{K_1 + \nu E} > N_0 \,, \qquad (19)$$

where, N_0 is the initial integrin expression. From this condition and using parameters in Table 1, there is a critical value ν_c, such

that,

$$v_c < \frac{\alpha}{N_0}, \quad (20)$$

for increasing integrin expression to occur and above the critical value the integrin expression equation (5) becomes a decreasing function. With the choices of $\alpha = 0.15$ and $N_0 = 4$, the critical value must be $v_c < 0.0375$.

3.5 Varying EGF Secretion and Diffusion

The main purposes of experiments in [37] are to show that mechanical stretch increased EGF concentration in the wound healing system and increasing EGF concentration promoted an asymmetric migration pattern, where the speed of keratinocytes under the influence of EGF was slower than the speed of keratinocytes without being affected by EGF. To study how EGF secreted by fibroblasts affects keratinocyte migration in wound healing, we vary two aspects in the formulation of EGF in equation (16): the diffusion coefficient D_E and secretion ϕ. For simplicity, linear Fickian diffusion is assumed to govern the propagation of EGF field in the keratinocyte-fibroblast system.

The first aspect we want to explore is EGF secretion, where, increasing EGF secretion resembles increasing EGF concentration by applying mechanical stretch in the experiments. To examine the impact of EGF secretion by fibroblasts in a wound healing system, we vary ϕ in equation (16). Decreasing the production of EGF 10 times lower than its default value (from $\phi = 0.2$ to $\phi = 0.02$) causes keratinocytes that have decelerated due to high EGF secretion to pick up their migration speed, as can be seen in the top row figures of Figure 15. At high integrin-ligand binding affinity $k_{Int,Coll} = -1.5$, lowering EGF secretion results in acceleration of keratinocyte migration moving to the right. This indicates that surface tension that is already low when $\phi = 0.2$ becomes even lower (very weak), leading to faster migration. Low surface tension in our model is related to low integrin expression. We observe similar effect of acceleration at low integrin-ligand binding affinity $k_{Int,Coll} = -2.0$. However, with $k_{Int,Coll} = -2.0$, cells could have both positive and negative surface tension as integrin expression is varied. Decreasing secretion rate suggests that the elevation of integrin density is slow, hence, relaxing the increment of surface tension. As we estimated, the opposite effect takes place if EGF secretion is increased to $\phi = 20.0$, where we observe that keratinocyte moving to the right experiences very high EGF concentration earlier which causes speed deceleration due to abrupt integrin density elevation, where the slope in equation (5) becomes steep. In these simulations with EGF secretion variation, all other parameters are kept as in Table 1. For comparison, simulation results with default secretion rate $\phi = 0.2$ (dashed blue and yellow lines for keratinocyte moving to the left and right, respectively) are superimposed in Figure 15. These simulations prove the key point of our experiments mentioned above, that increasing EGF secretion indeed promotes asymmetric migration pattern.

Based on the layout of keratinocytes and fibroblasts described in [37], we presume that EGF diffusion can be another factor that may influence keratinocyte migration. Increasing EGF diffusion in the wound healing system signifies fast propagation of EGF field

from fibroblasts toward keratinocytes, hence keratinocytes moving toward fibroblasts perceive high EGF concentration at early times. It leads to the occurrence of early speed deceleration, as shown in Figure 16. For comparison, simulation results using the default parameter $D_E = 0.25$ are also plotted in Figure 16.

In all simulation results presented in Figures. 14, 15, and 16, the quantity of EGF in the system differs in each scenario (default parameters, higher secretion rate, and higher diffusion coefficient, respectively). Since EGF concentration controls the expression of integrin receptors on the surface of keratinocytes, the amount of expressed integrin density also varies depending on EGF secretion or diffusion. In Figure 17, integrin expression of a keratinocyte moving to the right is plotted as a function of EGF concentration perceived by the same cell. In general, the relation between EGF concentration and integrin expression forms a saturation growth rate-like function for all simulations, as formulated in equation (5). This is corroborated by simulation outputs, as shown in the figure plots of Figure 17. In Figure 17, the steepness of each line is related to the values of $k_{Int,Coll}$, where less steep slopes correlate with high integrin-ligand binding affinity $k_{Int,Coll}$ and more steeper slopes correlate with low $k_{Int,Coll}$.

3.6 Varying Integrin-Ligand Binding Affinity

In addition to varying integrin expression, our model also allows the alteration of integrin-ligand binding affinity, which here, is performed in the middle of simulation. An example use of altering integrin-ligand binding affinity mid-simulation is to restore cell motility from restrained migration. When keratinocyte speed decelerates and cells eventually cohere, migration speed can be restored by altering (or reducing) EGF secretion and diffusion, as shown in Figs. 15 and 16. These strategies only work if we have prior knowledge that EGF secretion and diffusion are high enough to induce rapid integrin increase. However, from our simulation results which are not shown in this paper, if integrin expression is already at its maximal density, reducing EGF secretion or diffusion mid-simulation has no effect in keratinocyte speed and cells cease to move forward. One of several solutions we propose here is to steer integrin-ligand binding affinity in the middle of simulation, among others. We know from the relationship between surface tension and integrin expression in Figure 10 that high integrin-ligand binding affinities bound to very low surface tension, where, cell motility is high. Simulation results using this steering strategy at high EGF secretion rate, $\phi = 20.0$, are shown Figure 18. Figures in the left column show keratinocytes moving to the right that have been restrained from migrating, whereas figures in the right column shows keratinocytes that have stopped moving on day 3 regain their motility after integrin-ligand binding affinity is switched from $k_{Int,Coll} = -2.0$ to $k_{Int,Coll} = -1.0$ slightly after day 3, when cohesion is perceived. In the insert figure of right plots, surface tension of keratinocytes moving to right continuously increases and transitions from negative to positive (red line), indicating deceleration and eventually no migration. When $k_{Int,Coll}$ is switched from -2.0 to -1.0, surface tension abruptly drops from positive to negative (blue line). To prove that steering $k_{Int,Coll}$ mid-simulation may help to reinstate cell speed, in this

paper we only apply a step function for switching $k_{\text{Int,Coll}}$ values although it is possible to use other functions that are more dynamics.

3.7   Fitting Simulation Results To Experimental Data

For data fitting in this subsection and cell spreading patterns in the next subsection, we ran simulations using a different set of parameters than those in Table 1. In these simulations, we reduced target volume to $V_t = 16$ and excluded surface constraint ($\lambda_\sigma^{\text{surf}} = 0$), hence taking only volume constraint contribution in the size constraint. E-cadherin-E-cadherin binding affinity was also increased to $k_{\text{Ecad,Ecad}} = -10.0$. Changes in adhesion energies surely affect cell migration speed and if these changes are combined with changes in size constraint, the effective energy H is also affected. Based on the new parameters, the total ef-fective energy became lower because size constraint was smaller. The new value of $k_{\text{Ecad,Ecad}}$ changed the total adhesion energy, and it shifted the predicted surface tension spectrum in Figure 10 around 6 units up, where the minimum surface tension with $k_{\text{Int,Coll}} = 1.5$ (blue line) was now around -14. Increased sur-face tension, as we know, leads to slower migration speed. Ex-cluding surface constraint may give rise to cell fragmentation if membrane fluctuation is too high. Hence, now we reduced the amplitudes of membrane fluctuation for both keratinocytes and fibroblasts to $T_{m,k} = 25$ and $T_{m,f} = 5$, respectively. Each data set is comparable with different values of D_E and ϕ. Other parameters remained the same as in Table 1. With the new parameter set, time scale was also altered, where now 1 MCS $\sim$ 3 minutes or 480 MCS $\sim$ 1 day. Letting cells grow for around 100 MCS, day 1 was measured at 580 MCS, day 2 at 1060 MCS, and day 6 at 2980 MCS.

Using the new parameter set, we compare select simulation results with data from our previous work in[37] and data from studies in[36]. From data that have been described in the Materials and Methods section in Figure 3, we compare the results of co-culture experiments in cases 3 and 4 with our computational simulations. Case 3 is co-culture experiments without mechanical stretch or without EGF production enhancement, therefore keratinocytes migrating to the right (toward fibroblasts) and to the left (away from fibroblasts) approximately have the same migration speeds because EGF is so small and has no effect on these cells. Whereas, case 4 is co-culture experiments with mechanical stretch or EGF enhancement resulting in speed difference between the right-moving and left-moving keratinocytes.

Plots in Figure 19 show the comparison between data and sim-ulation results. The results using low integrin-ligand binding affinities, $k_{\text{Int,Coll}} = -2.5$ and $k_{\text{Int,Coll}} = -3.0$, seem to be in a good agreement with the non-stretched co-culture experiments, shown by figures in the left column. Biologically, low integrin-ligand binding affinity could be caused by growth factor (or EGF) defi-ciency that weakens cell-matrix adhesion and subsequently slows down cell migration. Simulations with higher binding affinity, $k_{\text{Int,Coll}} = -1.5$ and $k_{\text{Int,Coll}} = -2.0$, are comparable with case 4, right column of Figure 19. Most of simulation results appear to be close to data on days 5 and 6, whereas results on days 1, 2, 3 somehow deviate from data because cell speed is very high due

to small adhesions (or low integrin expression) used by cells on the first few days.

Stefonek-Puccinelli and Masters in their studies measured av-erage cumulative migration of keratinocytes for various EGF concentrations and gradients[36]. One of their experimental re-sults showed that the speed of keratinocytes migrating on 2D substrates injected with different EGF concentrations (83, 167, 333, and 667 μg/mL) was optimal at concentration 167 μg/mL, whereas at higher concentrations (333 and 667 μg/mL) ker-atinocyte migration speed declined with the slowest speed oc-curred at the highest concentration, 667 μg/mL. We compare our tracked right-moving keratinocyte with keratinocyte moving on 667 μg/mL EGF in[36] and the left-moving keratinocyte with keratinocyte moving on 167 μg/mL EGF in[36]. The fitting is shown in Figure 20, where the results are also comparable. Note that keratinocytes in Stefonek-Puccinelli and Masters' studies are slower than keratinocytes in our experiments in[37], hence the fit-ting matches with simulations with lower ligand-binding affini-ties, $k_{\text{Int,Coll}} = -2.5$ and $k_{\text{Int,Coll}} = -3.0$.

Stefonek-Puccinelli and Masters also measured average cumu-lative migration of keratinocytes when migrating on substrates in-jected with different concentrations and gradients of insulin-like growth factor-1 (IGF-1)[36]. Their results with different gradients of IGF-1 but the same IGF-1 concentration (150 μg/ml) are shown on the left of Figure 21 and results with different IGF-1 concen-trations using quadratic gradient are shown on the right. These experimental results show migration patterns that are similar to our simulations result with high EGF secretion and diffusion ex-hibiting cell cohesion and a biphasic behavior. Because the cumu-lative migration distances in their results are short compared to our simulation results, we don't show plots of comparison with our simulation results here. However, our simulation results are only qualitatively comparable with their results.

3.8   Cell Spreading Patterns

Without external stimuli, varying cell adhesion energies by vary-ing either one of the components of adhesion such as integrin expression level, ligand level, and integrin-ligand binding affin-ity or all of them altogether can result in cells migrating in a nonuniform manner resembling finger-like morphology, as seen in Figure 22(A) and (B). The fingering of epithelial cells has been observed in wound healing and studied experimentally using Madin-Darby canine kidney (MDCK) cells[103–105]. In all patterns in Figure 22, integrin expression is regulated by equation (17) with $\omega = 0.01$, initial integrin expression $N_\sigma^{\text{Int}}(t = 0) = 0.1$, and E-cadherin is taken to be constant $N_\sigma^{\text{Ecad}} = 6.4$. Similar to mono-culture simulations, the constant expression of collagen will take place when integrin expression level reaches $N_\sigma^{\text{Int}} = 15$ due to the minimum function in equation (4), which occurs after 1490 MCS. All images were taken at 10,000 MCS when the patterns have sta-bilized from increasing integrin expression. The most noticeable fingering pattern is observed with $k_{\text{Int,Coll}} = -2.4$, where surface tension increases from around $\gamma = -31.7$ and after 1490 MCS re-mains at a positive constant $\gamma = 4.0$. From their initial position (set similar to monoculture simulations), cells spread outwardly
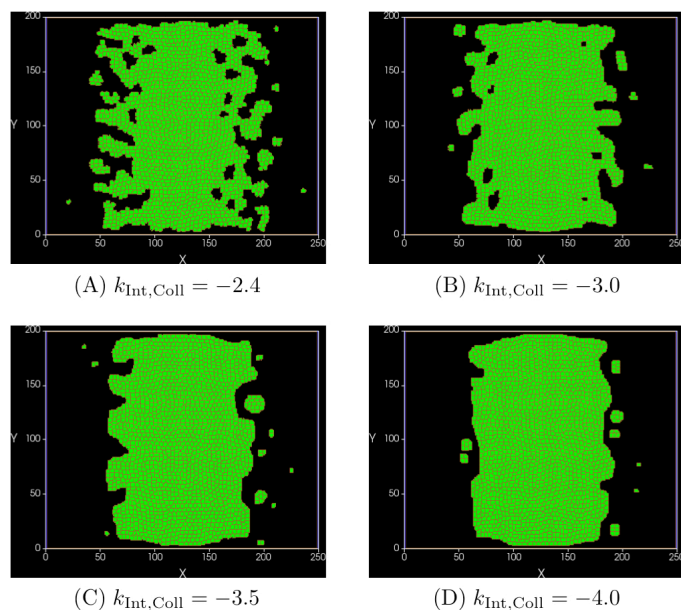
Fig. 22 Variations of keratinocyte migration pattern by varying $k_{\text{Int,Coll}}$. Patterns generated from letting linear integrin expression, as in equation (17), without being influenced by EGF with varying integrin-ligand binding affinity taken at 3460 MCS or around 7 days. Initial integrin and E-cadherin densities are taken to be 0.1 and 6.4, respectively.

and individually due to negative surface tension. When surface tension becomes positive, cells start to form finger-like columns which are an outcome of cell-matrix energy that is slightly higher than cell-cell adhesion energy, or cell-matrix attachments that are slightly weaker than cell-cell attachments. The finger-like morphology, in particular as a result of integrin over-expression, has been observed experimentally on keratinocyte cells[106]. However, if surface tension is increased, for example by using $k_{\text{Int,Coll}} < -3.0$ as in Figure 22(C) and (D), less protruding or fingering pat-tern will occur because cell-matrix adhesion energy will be much higher than cell-cell adhesion energy, resulting in much stronger cell-cell attachments and cell coherence.

4 Discussion and Conclusions

Cutaneous wound repair is a dynamic process that involves highly integrated cellular and molecular events, which all must take place in the proper sequence and time frame in order to permit successful healing. Keratinocyte cells are a major component of the skin epidermal layer where their effective migration within the skin structures is critical for successful covering the denuded epithelial layer that can be caused by injury or diseases. Numerous growth factors have been shown to stimulate the migration of epidermal keratinocytes[11,107]. Members of epidermal growth factor (EGF) family, comprising EGF itself, transforming growth factor-α (TGF-α), and heparin binding epidermal growth factor (HB-EGF), are considered the key regulators of keratinocyte migration at the wound margin[107]. However, some studies also showed that growth factors can have another opposite effect on epidermal keratinocytes, where their high concentration through over-secretion or over-production can slow down and eventually

cease keratinocyte migration. Decreased keratinocyte migration is a distinct feature of delayed re-epithelialization which impairs wound healing progresses and renders to chronic non-healing wounds. In this case, immotile keratinocytes may not be able to maintain epidermal skin barriers and close open wound. It may also contribute to wound reoccurrence, which is a significant clinical problem[6].

In this paper, we have formulated a model of keratinocyte migration for re-epithelialization of the wound healing process. In our study, paracrine signaling between EGF secreted by fibroblasts and integrin expression of nearby keratinocytes is implicated in the obstruction of keratinocyte migration. Overly high EGF concentration causes deceleration of keratinocyte migration due to the biphasic dependence of keratinocyte migration speed on integrin expression that subsequently leads to delayed re-epithelialization, impeding the wound healing process.

The seemingly polarized studies of the relations between EGF and integrin expression for cell migration, where one group of studies opines that EGF stimulates integrin expression, leading to increased cell migration, and the other group implicates EGF in cell migration deceleration, are not in conflict with each other. It is actually the consequences of the biphasic feature of cell migration speed on different EGF concentrations. Some experimental data have observed and reported that the response of cell migration to EGF is dose dependent[14,29,108], meaning that EGF can both increase and decrease the migration speed of individual cells in a population. However, there exists a range of maximal stimulation concentrations, where low EGF concentrations stimulate migration[109–111], but relatively high EGF concentrations inhibit cells migration[29,57,108,112]. Experimental results by Chen et al[29] displayed the biphasic behavior shown in the plots of cell migration index in different ranges of EGF concentration (0, 0.001, 0.01, 0.1, 1 ng/ml). In their study, keratinocyte migration index seemed to be optimal at around 0.01 ng/ml rEGF for migration on type-I collagen. The biphasic behavior is also observed in another study by Maldonado and Furcht[35] where they measured the migration of human corneal epithelial cells on fibronectin. With the EGF concentration range between 0.01 to 40 ng/ml, the migration speed of human corneal epithelial cells was optimal at 5 and 10 ng/ml. Above 10 ng/ml the migration decreased. Studies by Stefonek-Puccinelli and Masters[16,36] whose results we use for data fitting in this paper also showed the biphasic effect by using different gradient shapes and concentration levels of EGF. A work by Wang et al[113] also showed that cell migration depends on the shape of gradient profile of EGF stimulation and on the range of EGF concentrations. Thus, experimental results showed that EGF regulation of cell migration in wound regeneration was biphasic dependence.

The novelty of our work mostly lies in the successful prediction of dynamic process of keratinocytes migration and elucidating the combination of biochemical and mechanical aspects of cell migration underlying the mechanisms of keratinocyte migration in the presence of fibroblasts based on our previous experiments[37]. Keratinocyte migration in our model is governed by EGF secreted by fibroblasts through paracrine signaling and implemented in the CPM, one of the lattice-based individual cell-based frameworks.

Individual cell-based method has been used to model wound healing since at least the last 10 years[114–118]. Our simulation results suggest that there are three components that regulate keratinocyte migration: (i) cell-matrix adhesion which is governed by integrin-ligand binding affinity, (ii) EGF diffusion, and (iii) the amount of EGF secretion or production by fibroblasts. Varying the parameters of these components together can either accelerate or decelerate keratinocyte migration.

For sure there is room for improvement of our model. To make it more realistic, several things can be taken into account, for example, by having stochastic function for the EGF secretion and integrin expression (in equation (5)), or by incorporating cell-cell adhesion mechanics and biochemistry, intracellular pathways connecting EGF and integrins, improvement of surface tension formulation, or adding keratinocyte proliferation. A detailed molecular model of integrin expression levels that produce different adhesion structures such as nascent adhesions, focal complexes, focal adhesions, and fibrillar adhesions where biphasic dependence of cell speed on these structures can be visibly captured, may also be another interesting future project. For better model fittings, experimental data to obtain parameters in our model are also necessary.

There is an urgent need for developing effective therapy to stimulate cellular activity for wound patients. Sequential and efficient wound healing is monitored by intercellular communication, mainly via growth factors and cytokines. Based on the recognition of their implications in wound healing, growth factors have been proposed as therapeutic agents for wound repair and growth factor therapy has been acknowledged in clinical practices for wound treatments[119]. Animal studies have also confirmed that growth factors can promote and enhance wound healing, in which the products containing platelet-derived growth factor (PDGF), basic fibroblast growth factor (bFGF), and EGF have already being applied in clinical settings. There are EGF-based wound healing products for chronic and burn wounds that are currently marketed worldwide. EGF, along with PDGF and FGF, has been commercially produced into gel and aqueous solution for topical use on ulcers[120]. EGF is also used as a therapeutic drug to treat diabetic ulcers in South Korea and to cure corneal ulcers as eye drops in Belgium. EGF can be applied through intralesional injection in an effective and safe way to enhance advanced diabetic foot ulcer healing and reduces the risk of major amputation without dose dependency[121]. A study shows that, however, only a modest improvement appeared and the topical application of EGF in human impaired of venous ulcers failed to significantly enhance re-epithelialization[122]. Delayed re-epithelialization in such study could be attributed to EGF concentration used in the treatments, based on our own study. However, it should be pointed out that more *in vivo* and *in vitro* studies are needed to confirm the capability of growth factors in delaying wound healing through the biphasic behavior, and further investigations are required to verify our finding. While a large number of investigations have been focused on the effect of mechanical loading on keratinocyte proliferation and the corresponding molecular mechanisms, more new ideas and explanation also need in theoretical and clinical research.

Conflicts of interest

All authors declare no competing financial interests.

Acknowledgements

Author contributions statement

V.A. wrote the paper and performed the simulations, V.A. and F.S. formulated the mathematical model, V.A. and M.S. arranged the computational scheme for simulations, V.A., D.L., M.S., S.F., M.Z., and M.L. analyzed the results, D.L., S.F., L.C., X.L., and M.L. conducted the experiments.

References

1 T. Velnar, T. Bailey and V. Smrkolj, *J Int Med Res*, 2009, **37**, 1528–1542.

2 C. E. Fife, M. J. Carter, D. Walker and B. Thomson, *Wounds*, 2012, **24**, 10–17.

3 S. Guo and L. A. DiPietro, *J Dent Res*, 2010, **83**, 219–229.

4 M. J. Escámez, M. García, F. Larcher, A. Meana, E. Muñoz, J. L. Jorcano and M. Del Río, *J Invest Dermatol*, 2004, **123**, 1182–1191.

5 H. Ramirez, S. B. Patel and I. Paster, *Adv Wound Care*, 2014, **3**, 482–491.

6 I. Pastar, O. Stojadinovic, N. C. Yin, H. Ramirez, A. G. Nusbaum, A. Sawaya, S. B. Patel, L. Khalid, R. R. Isseroff and M. Tomic-Canic, *Adv Wound Care (New Rochelle)*, 2014, **3**, 445–464.

7 K. Hashimoto, *J Dermatol Sci*, 2000, **24**, S46–S50.

8 R. Gillitzer and M. Goebeler, *J Leukoc Biol*, 2001, **69**, 513–521.

9 Y. Shirakata, *J Dermatol Sci*, 2010, **59**, 73–80.

10 P. V. Peplow and M. P. Chatterjee, *Cytokine*, 2013, **62**, 1–21.

11 M. A. Seeger and A. S. Paller, *Adv Wound Care*, 2015, **4**, 213–224.

12 M. Laato, J. Niinikoski, L. Lebel and B. Gerdin, *Ann Surg*, 1986, **203**, 379–381.

13 L. B. Nanney, *J Invest Dermatol*, 1990, **94**, 624–629.

14 H. Chiba, T. Kazama, Y. Yamamoto, T. Suyama and M. Ito, *Acta Med Biol*, 2003, **51**, 31–41.

15 I. Haase, R. Evans, R. Pofahl and F. M. Watt, *J Cell Sci*, 2003, **116**, 3227–3238.

16 T. J. Stefonek and K. S. Masters, *Wound Rep Reg*, 2007, **15**, 847–855.

17 M. Blumenberg, *BMC Genomics*, 2013, **14**, 85.

18 E. B. Tredget, J. Demare, G. Chandran, E. E. Tredget, L. Yang and A. Ghahary, *Wound Repair Regen*, 2005, **13**, 61–67.

19 M. Pakyari, A. Farrokhi, M. K. Maharlooei and A. Ghahary, *Adv Wound Care*, 2013, **2**, 215–224.

20 S. Werner, *Am J Pathol*, 2011, **179**, 2144–2147.

21 M. Meyer, A. K. Müller, J. Yang, D. Moik, G. Ponzio, D. M.

Table 1 Model parameters

Parameter description	Symbol	Value	Unit
Lattice dimension for monoculture simulations		$300 \times 200 \times 1$	pixels
Lattice dimension for co-culture simulations		$450 \times 200 \times 1$	pixels
Keratinocyte's cell membrane fluctuation	$T_{m,k}$	80	Joules [96]
Fibroblast's cell membrane fluctuation	$T_{m,f}$	7	Joules [96]
Pixel copy order neighbor		2 or 3	—
Cell's target volume	V_t	20.0	pixels
Cell's target surface	S_t	20.0	pixels
Lambda volume	$\lambda_\sigma^{\text{vol}}$	25.0	
Lambda surface	$\lambda_\sigma^{\text{surf}}$	15.0	
Keratinocyte's base integrin density	N_σ^{Int}	4	receptors/area
Keratinocyte's E-cadherin density	N_σ^{Ecad}	4	receptors/area
Fibroblast's integrin density	N_σ^{Int}	4	receptors/area
Fibroblast's E-cadherin density	N_σ^{Ecad}	4	receptors/area
Collagen density in `Medium`	N_σ^{Coll}	15.0	molecules/area
E-cadherin-E-cadherin binding affinity	$k_{\text{Ecad,Ecad}}$	-13.0	M
Integrin-Collagen binding affinity	$k_{\text{Int,Coll}}$	$-1.5, -2.0, -2.5, -3.0$	M
Adhesion between `Keratinocyte` and `Wall`	$J_{\text{k,wall}}$	250.0	Joules/area
Adhesion between `Fibroblast` and `Wall`	$J_{\text{f,wall}}$	250.0	Joules/area
EGF diffusion constant	D_E	0.25	pixels^2/MCS
EGF production rate by fibroblasts	ϕ	0.2	nM (pixels MCS)$^{-1}$
EGF production rate by keratinocytes	β	0 and 0.0005	nM (pixels MCS)$^{-1}$
EGF decay rate	η	0.0024	MCS^{-1}
Constant in integrin density equation (5)	α	0.15	
Constant in integrin density equation (5)	ν	0.01	
Constant in integrin density equation (5)	θ	1	
Constant in integrin density equation (5)	K_1	1	
Constant in integrin density equation (5)	r	1	

Integrative Biology Accepted Manuscript

Ornitz, R. Grose and S. Werner, *J Cell Sci*, 2012, **125**, 5690–5701.

22 S. Werner, H. Smola, X. Liao, M. T. Longaker, T. Krieg, P. H. Hofschneider and L. T. Williams, *Science*, 1994, **266**, 819–822.

23 Y. P. Xia, Y. Zhao, J. Marcus, P. A. Jimenez, S. M. Ruben, P. A. Moore, F. Khan and T. A. Mustoe, *J Pathol*, 1999, **188**, 431–438.

24 M. Marikovsky, P. Vogt, E. Eriksson, J. S. Rubin, W. G. Taylor, S. Joachim and M. Klagsbrun, *J Invest Dermatol*, 1996, **106**, 616–621.

25 R. Blakytny, E. B. Jude, J. M. Gibson, A. J. Boulton and M. W. Ferguson, *J Pathol*, 2000, **190**, 589–594.

26 R. A. Achar, T. C. Silva, E. Achar, R. B. Martines and J. L. Machado, *Acta Cir Bras*, 2014, **29**, 125–131.

27 J. Gailit, M. P. Welch and R. A. Clark, *J Invest Dermatol*, 1994, **103**, 221–227.

28 G. Zambruno, P. C. Marchisio, A. Marconi, C. Vaschieri, A. Melchiori, A. Giannetti and M. De Luca, *J Cell Biol*, 1995, **129**, 853–865.

29 J. D. Chen, J. P. Kim, K. Zhang, Y. Sarret, K. C. Wynn, R. H. Kramer and D. T. Woodley, *Exp Cell Res*, 1993, **209**, 216–223.

30 Q. H. Song, R. P. Singh and V. Trinkaus-Ranvall, *J Cell Biochem*, 2001, **80**, 397–414.

31 A. Watson, V. L. Morris and B. M. Chan, *Arch Dermatol Res*, 2009, **301**, 307–317.

32 D. Y. Lü, Z. Li, X. Y. Gao, C. H. Luo, F. Zhang, L. Zheng, J. W. Wang, S. J. Sun and M. Long, *Biomed Eng*, 2016, **15**, 605–620.

33 L. Häkkinen, L. Koivisto, H. Gardner, U. Saarialho-Kere, J. M. Carroll, M. Lakso, H. Rauvala, M. Laato, J. Heino and H. Larjava, *Am J Pathol*, 2004, **164**, 229–242.

34 S. AlDahlawi, A. Eslami, L. Häkkinen and H. S. Larjava, *Wound Repair Regen*, 2006, **14**, 289–297.

35 B. A. Maldonado and L. T. Furcht, *Invest Ophthalmol Vis Sci*, 1995, **36**, 2120–2126.

36 T. J. Stefonek-Puccinelli and K. S. Masters, *Ann Biomed Eng*, 2008, **36**, 2121–2133.

37 D. Lü, X. Liu, Y. Gao, B. Huo, Y. Kang, J. Chen, S. Sun, L. Chen, X. Luo and M. Long, *PLoS ONE*, 2013, **8**, e74563.

38 N. Solic and D. E. Davis, *Exp Cell Res*, 1997, **234**, 465–476.

39 H. T. Zhang, M. Gorn, K. Smith, A. P. Graham, K. Lau and R. Bicknell, *Angiogenesis*, 1999, **3**, 211–219.

40 S. Smida Rezgui, S. Honore, J. B. Rognoni, P. M. Martin and C. Penel, *Int J Cancer*, 2000, **87**, 360–367.

41 K. Danker, N. Mechai, L. Lucka, W. Reutter and R. Horstkorte, *Biol Chem*, 2001, **382**, 969–972.

42 N. Pouliot, E. C. Nice and A. W. Burgess, *Exp Cell Res*, 2001, **266**, 1–10.

43 B. A. Lessey, *Ann NY Acad Sci*, 2002, **955**, 265–280.

44 Y. Nakatsuji, Y. Nishio, N. Tani, K. Adachi, M. Ohmichi, K. Hisamoto, K. Morishige, H. Kurachi, K. Tasaka, Y. Murata and N. Matsuura, *Endocr J*, 2003, **50**, 703–714.

45 I. Yamanaka, M. Koizumi, T. Baba, S. Yamashita, T. Suzuki and R. Kudo, *Exp Cell Res*, 2003, **286**, 165–174.

46 Y. Mukoyama, A. Utani, S. Matsui, S. Zhou, Y. Miyachi and N. Matsuyoshi, *Genes Cells*, 2007, **12**, 787–796.

47 K. S. Hong, E.-Y. Jeon, S. S. Chung, K. H. Kim and R.-A. Lee, *Cancer Cell Int*, 2018, **18**, 32.

48 M. A. Adelsman, J. B. McCarthy and Y. Shimizu, *Mol Biol Cell*, 1999, **10**, 2861–2878.

49 A. Huttenlocher, M. H. Ginsberg and A. F. Horwitz, *J Cell Biol*, 1996, **134**, 1551–1562.

50 S. Schmidt and P. Friedl, *Cell Tissue res*, 2010, **339**, 83–92.

51 S. P. Palecek, J. C. Loftus, M. H. Ginsberg, D. A. Lauffenburger and A. F. Horwitz, *Nature*, 1997, **385**, 537–540.

52 F. G. Giancotti and R. Ruoslahti, *Cell*, 1990, **60**, 849–859.

53 P. J. Keely, A. M. Fong, M. M. Zutter and S. A. Santoro, *J Cell Sci*, 1995, **108**, 595–607.

54 A. Giese, M. A. Loo, S. A. Norman, S. Treasurywala and M. E. Berens, *J Cell Sci*, 1996, **109**, 2161–2168.

55 J. H. Chon, R. Netzel, B. M. Rock and E. L. Chaikof, *Ann Biomed Eng*, 1998, **26**, 1091–1101.

56 M. F. Ware, A. Wells and D. A. Lauffenburger, *J Cell Sci*, 1998, **111**, 2423–2432.

57 G. Maheshwari, A. Wells, L. G. Griffith and D. A. Lauffenburger, *Biophys J*, 1999, **76**, 2184–2823.

58 G. Maheshwari, G. Brown, D. A. Lauffenburger, A. Wells and L. G. Griffith, *J Cell Sci*, 2000, **113**, 1677–1686.

59 P. A. DiMilla, K. Barbee and D. A. Lauffenburger, *Biophys J*, 1991, **60**, 15–37.

60 P. A. DiMilla, J. A. Stone, J. A. Quinn, S. M. Albelda and D. A. Lauffenburger, *J Cell Biol*, 1993, **122**, 729–737.

61 L. Olsen, J. A. Sherratt and P. K. Maini, *J Theor Biol*, 1995, **177**, 113–128.

62 V. H. Barocas and R. T. Tranquillo, *J Biomech Eng Trans ASME*, 1997, **119**, 137–145.

63 D. M. Knapp, V. H. Barocas, A. G. Moon, K. Yoo, L. R. Petzold and R. T. Tranquillo, *J Rheol*, 1997, **41**, 971–993.

64 A. F. Laplante, L. Germain, F. A. Auger and V. Moulin, *FASEB J*, 2001, **15**, 2377–2389.

65 W. M. Longmate and C. M. DiPersio, *Adv Wound Care*, 2014, **3**, 229–246.

66 J. A. Glazier, A. Balter and N. J. Poplawski, *Single-Cell-Based Models in Biology and Medicine*, Birkhäuser Verlag, Basel, Switzerland, 2007, ch. II, pp. 79–106.

67 F. Graner and J. A. Glazier, *Phys Rev Lett*, 1992, **69**, 2013–2016.

68 J. A. Glazier and F. Graner, *Phys Rev E Stat Phys Plasmas Fluids Relat Interdiscip Topics*, 1993, **47**, 2128–2154.

69 N. B. Ouchi, J. A. Glazier, J.-P. Rieu, A. Upadhyaya and Y. Sawada, *Physica A*, 2003, **329**, 451–458.

70 J. L. Maître and C. P. Heisenberg, *Curr Opin Cell Biol*, 2011, **23**, 508–514.

71 D. J. Irvine, K. A. Hue, A. M. Mayes and L. G. Griffith, *Biophys J*, 2002, **82**, 120–132.

72 D. Coombs, M. Dembo, C. Wofsy and B. Goldstein, *Biophys J*, 2004, **86**, 1408–1423.

73 M. H. Swat, J. Belmonte, R. W. Heiland, B. L. Zaitlen, J. A. Glazier and A. Shirinifard, *CompuCell3D reference manual*, Biocomplexity Institute, Indiana University.

74 Y. D. Pan, K. Zhang, J. P. Qi, J. Yue, T. A. Springer and J. F. Chen, *Proc Natl Acad Sci USA*, 2010, **107**, 21388–21393.

75 H. B. Schiller and R. Fässler, *EMBO Rep*, 2013, **14**, 509–519.

76 P. W. Wiseman, C. M. Brown, D. J. Webb, B. Hebert, N. L. Johnson, J. A. Squier, M. H. Ellisman and A. F. Horwitz, *J Cell Sci*, 2004, **117**, 5521–5534.

77 J. M. Kowalewski, H. Shafqat-Abbasi, M. Jafari-Mamaghani, B. E. Ganebo, X. Gong, S. Strömblad and J. G. Lock, *PLoS ONE*, 2015, **10**, e0135204.

78 Z. Sun, S. S. Guo and R. Fässler, *J Cell Biol*, 2016, **215**, 445–456.

79 M. L. Gardel, I. C. Schneider, Y. Aratyn-Schaus and C. M. Waterman, *Annu Rev Cell Dev Biol*, 2010, **26**, 315–333.

80 B. Geiger, A. Bershadsky, R. Pankov and K. M. Yamada, *Nat Rev Mol Cell Biol*, 2001, **2**, 793–805.

81 C. K. Choi, M. Vicente-Manzanares, J. Zareno, L. A. Whitmore, A. Mogilner and A. R. Horwitz, *Nat Cell Biol*, 2008, **10**, 1039–1050.

82 J. T. Parsons, A. R. Horwitz and M. A. Schwartz, *Nat Rev Mol Cell Biol*, 2010, **11**, 633–643.

83 K. A. Beningo, M. Dembo, I. Kaverina, J. V. Small and Y. L. Wang, *J Cell Biol*, 2001, **153**, 881–888.

84 D. H. Kim and D. Wirtz, *Cell Adh Migr*, 2013, **7**, 293–296.

85 E. Dornier and J. C. Norman, *J Cell Biol*, 2017, **216**, 867–869.

86 B. Geiger and K. M. Yamada, *Cold Spring Harb Perspect Biol*, 2011, **3**, a005033.

87 D. A. Beysens, G. Forgacs and J. A. Glazier, *Can J Phys*, 2000, **78**, 243–251.

88 M. H. Swat, G. L. Thomas, A. Shirinifard, S. G. Clendenon and J. A. Glazier, *PLoS ONE*, 2015, **10**, e0127972.

89 R. David, O. Luu, E. W. Damm, J. W. H. Wen, M. Nagel and R. Winklbauer, *Development*, 2014, **141**, 3672–3682.

90 E. E. Robinson, K. M. Zazzali, S. A. Corbett and R. A. Foty, *J Cell Sci*, 2003, **116**, 377–386.

91 E. E. Robinson, R. A. Foty and S. A. Corbett, *Mol Biol Cell*, 2004, **15**, 973–981.

92 T. Caicedo-Carvajal, C. E. Shinbrot and R. A. Foty, *PLoS ONE*, 2010, **5**, e11830.

93 E. Genersch, D. Schuppan and R. B. Lichtner, *J Mol Med*, 1996, **74**, 609–616.

94 M. A. Deugnier, M. M. Faraldo, P. Roussell, J. P. Thiery and M. A. Glukhova, *J Cell Sci*, 1999, **112**, 1035–1044.

95 S. H. Zigmond, *Cell Motil Cytoskeleton*, 1993, **25**, 309–316.

96 J. Evans, W. Gratzer, N. Mohandas, K. Parker and J. Sleep, *Biophys J*, 2008, **94**, 4134–4144.

97 A. J. Kabla, *J R Soc Interface*, 2012, **9**, 3268–3278.

98 R. G. Thorne, S. Hrabetová and C. Nicholson, *J Neurophysiol*, 2004, **92**, 3471–3481.

99 G. Thurston, B. Jaggi and B. Palcic, *Cytometry*, 1988, **9**, 411–417.

100 K. R. Legate, S. A. Wickström and R. Fässler, *Genes Dev*, 2009, **23**, 397–418.

101 D. Vial and P. J. McKeown-Longo, *J Biol Chem*, 2012, **287**, 40371–40380.

102 M. H. Zaman, L. M. Trapani, A. L. Sieminski, D. Mackellar, H. Gong, R. D. Kamm, A. Wells, D. A. Lauffenburger and P. Matsudaira, *Proc Natl Acad Sci USA*, 2006, **103**, 10889–10894.

103 N. S. Gov, *Proc Natl Acad Sci USA*, 2007, **104**, 15970–15971.

104 M. Poujade, E. Grasland-Mongrain, A. Hertzog, J. Jouanneau, P. Chavrier, B. Ladoux, A. Buguin and P. Silberzan, *Proc Natl Acad Sci USA*, 2007, **104**, 15988–15993.

105 N. Yamaguchi, T. Mizutani, K. Kawabata and H. Haga, *Sci Rep*, 2015, **5**, 7656–7658.

106 P. v. d. Driesch, M. Fartasch, A. Hüner and M. Ponec, *Arch Dermatol Res*, 1995, **287**, 249–253.

107 G. Kirfel and V. Herzog, *Protoplasma*, 2004, **223**, 67–78.

108 Y. Hou, S. Hedberg and I. C. Schneider, *BMC Biophys*, 2012, **5**, 8.

109 Y. Ando and P. J. Jensen, *J Invest Dermatol*, 1993, **100**, 633–639.

110 J. E. Segall, S. Tyerech, L. Boselli, S. Masseling, J. Helft, A. Chan, J. Jones and J. Condeelis, *Clin Exp Metastasis*, 1996, **14**, 61–72.

111 Y. Li, J. Fan, M. Chen, W. Li and D. T. Woodley, *J Invest Dermatol*, 2006, **126**, 2096–2105.

112 G. Maheshwari, H. S. Wiley and D. A. Lauffenburger, *J Cell Biol*, 2001, **155**, 1123–1128.

113 S. J. Wang, W. Saadi, F. Lin, C. Minh-Canh Nguyen and N. Li Jeon, *Exp Cell Res*, 2004, **300**, 180–189.

114 S. R. McDougall, J. C. Dallon, J. A. Sherratt and P. K. Maini, *Philos Transact A Math Phys Eng Sci*, 2006, **364**, 1385–1405.

115 T. Sun, S. Adra, R. Smallwood, M. Holcombe and S. MacNeil, *PLoS ONE*, 2009, **4**, e8518.

116 S. Adra, T. Sun, S. MacNeil, M. Holcombe and R. Smallwood, *PLoS ONE*, 2010, **5**, e8511.

117 B. D. Cumming, D. L. S. McElwain and Z. Upton, *J R Soc Interface*, 2010, **7**, 19–34.

118 J. Arciero and D. Swigon, *Complex Systems and Computational Biology Approaches to Acute Inflammation*, Springer, New York, 2013, ch. III, pp. 185–207.

119 J. Hardwicke, D. Schmaljohann, D. Boyce and D. Thomas, *The Surgeon*, 2008, **6**, 172–177.

120 S. K. Han, *Innovations and advances in wound healing*, Springer-Verlag, Berlin, 2016, ch. 9, pp. 201–213.

121 J. I. Fernández-Montequín, E. Infante-Cristiá, C. Valenzuela-Silva, N. Franco-Pérez, W. Savigne-Gutierrez, H. Artaza-Sanz, L. Morejón-Vega, C. González-Benavides, O. Eliseo-Musenden, E. García-Iglesias, J. Berlanga-Acosta, R. Silva-Rodríguez, B. Y. Betancourt, P. A. López-Saura and C. C.-P. S. Group, *Int Wound J*, 2007, **4**, 333–343.

122 V. Falanga, W. H. Eaglstein, B. Bucalo, M. H. Katz, B. Harris and P. Carson, *J Dermatol Surg Oncol*, 1992, **18**, 604–606.
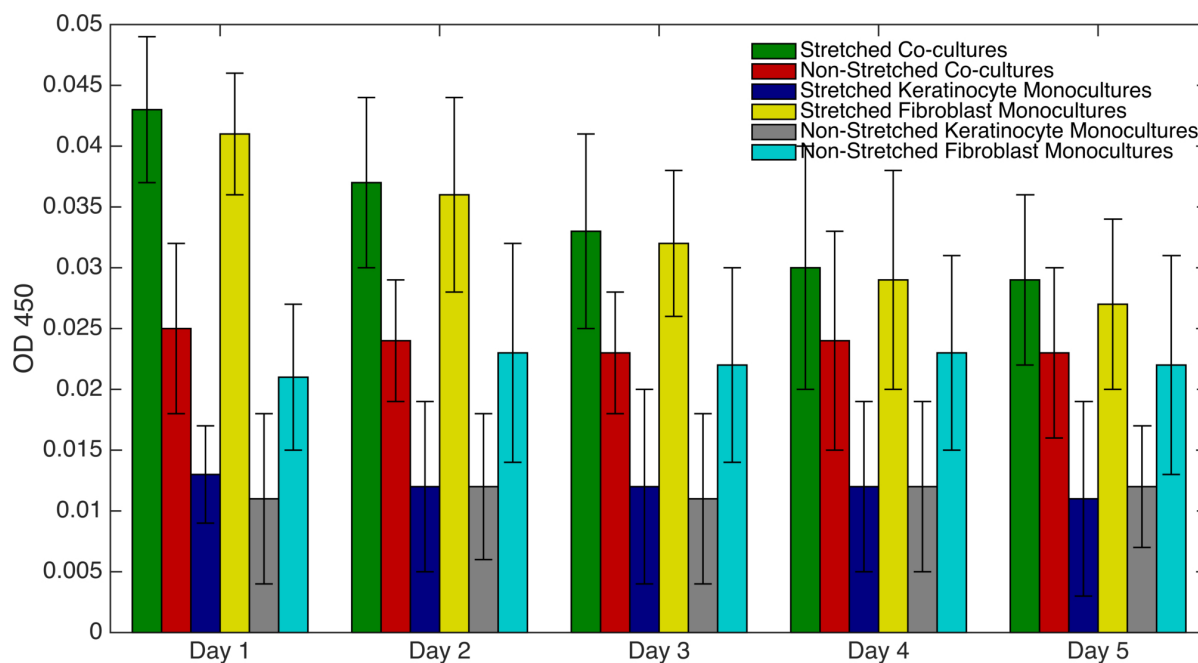
Fig. 1 Daily secretion of mean EGF content. Bar graph of mean EGF content measured from day 1 until day 5, reproduced from[37], for fibroblast monocultures (cyan), keratinocyte monocultures (gray), stretched fibroblast monocultures (yellow), stretched keratinocyte monocultures (navy blue), co-cultures (red), and stretched co-cultures (green). Each content is plotted with standard deviation with $n = 3$.
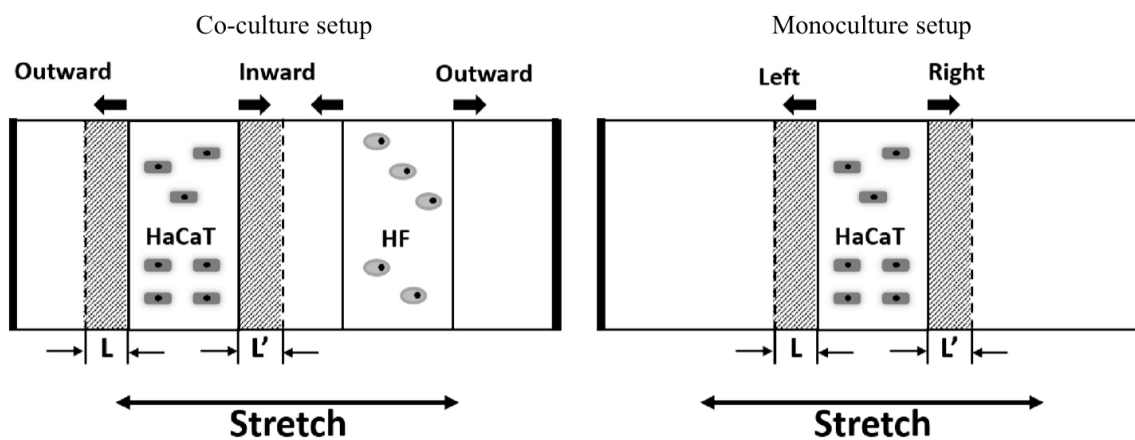
Fig. 2 Schematic illustration for monoculture (right) and co-culture (left) experiments on the stretched membrane. For monoculture experiments, either keratinocyte (HaCaT) cells or fibroblast (HF) cells are placed at the center of the membrane. For co-culture experiments, keratinocytes (HaCaT) are placed on the left of fibroblasts (HF). This schematic illustration is reproduced from[37].

(a) Case 1: Non-stretched monocultures

(b) Case 2: Stretched monocultures

(c) Case 3: Non-stretched co-cultures

(d) Case 4: Stretched co-cultures
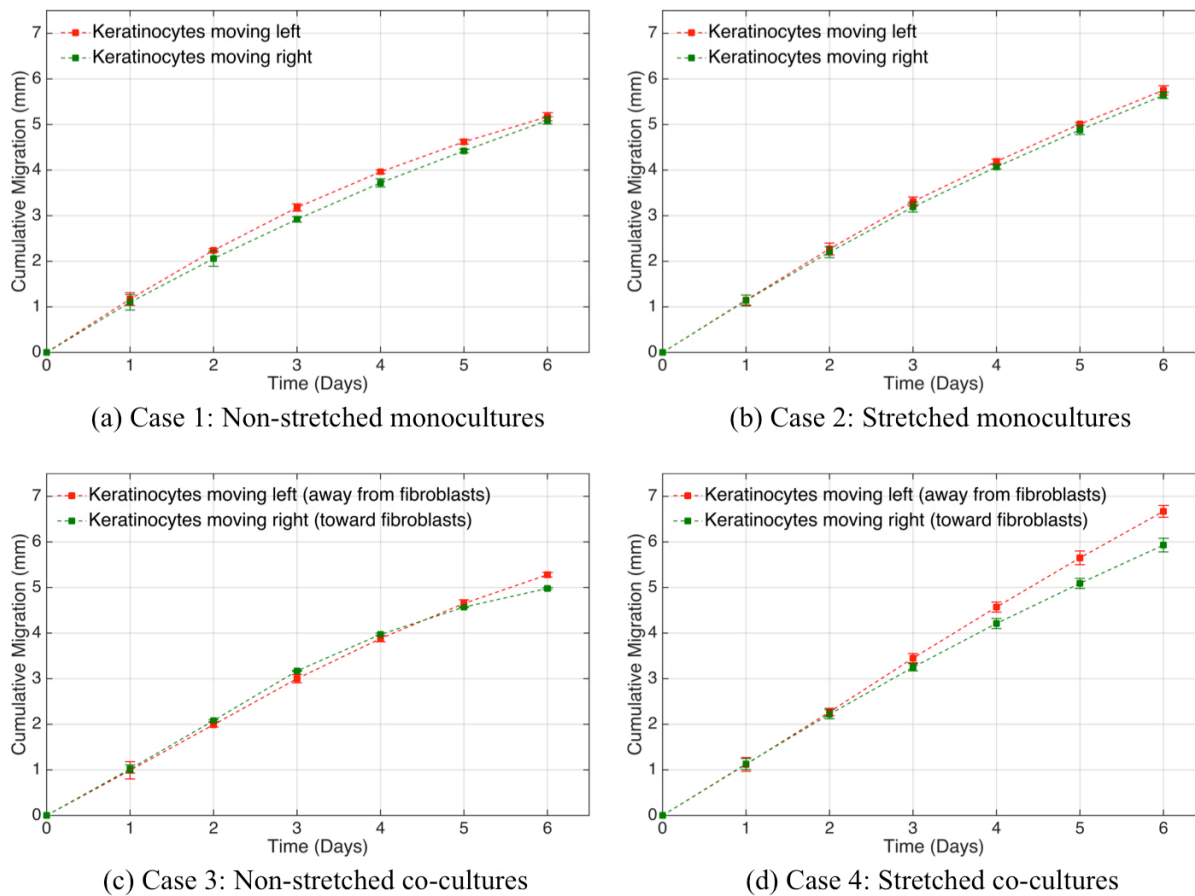
Fig. 3 Average cumulative migration of keratinocytes. Plots showing cumulative distances of keratinocytes moving toward fibroblasts (green) and keratinocytes migrating away from fibroblasts (orange), in monocultures without mechanical stretch (a), monocultures with mechanical stretch (b), co-cultures with fibroblasts without mechanical stretch (c), and co-cultures with fibroblasts with mechanical stretch (d). Data is reproduced from [37].
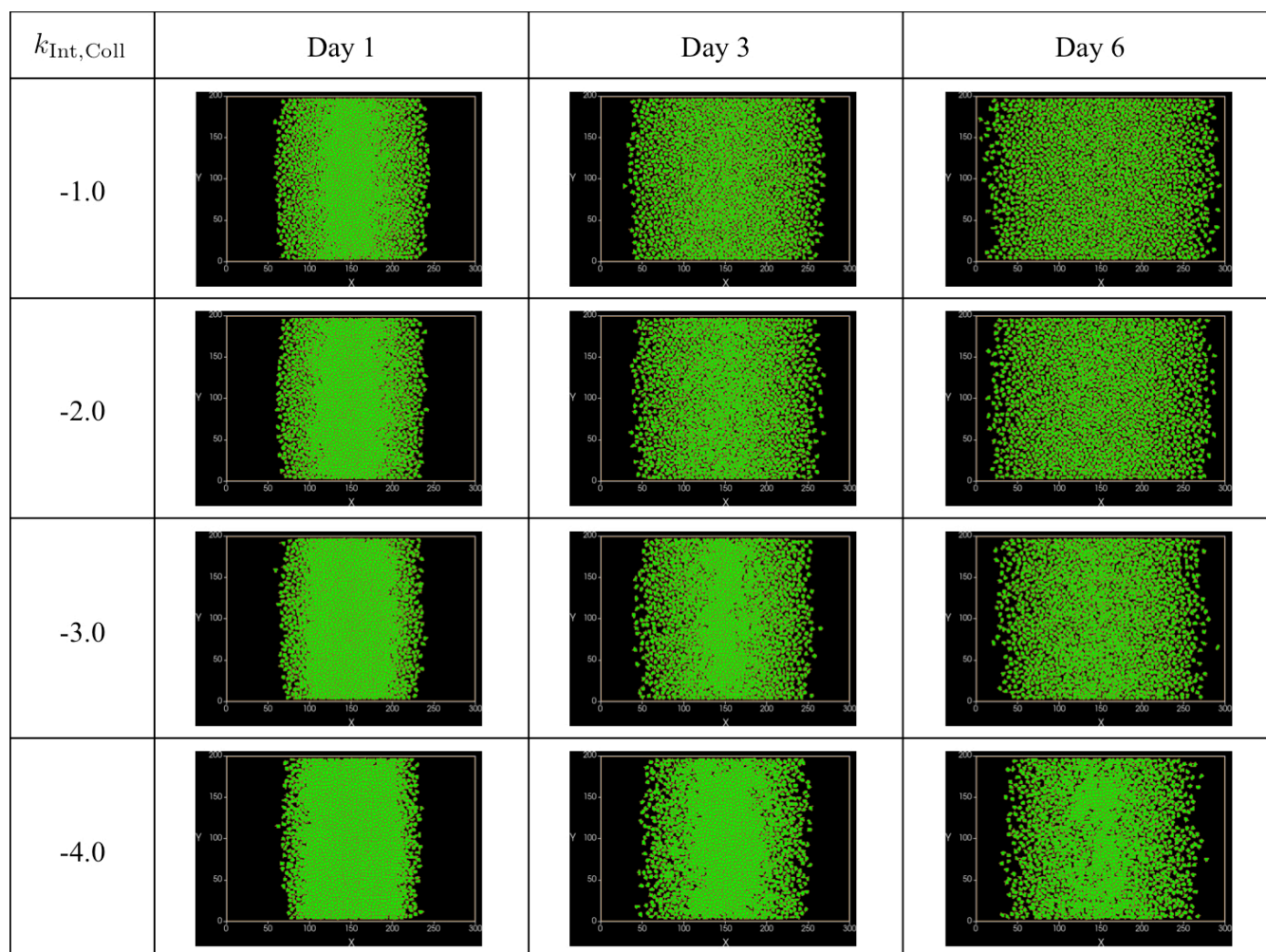
Fig. 6 Simulation results of monoculture keratinocytes with constant integrin expression. Screenshots showing migrating keratinocytes with membrane fluctuation $T_{m,k} = 80$ and constant integrin expression. Top row figures show monoculture keratinocytes when integrin-ligand binding is very high, that is at $k_{\text{Int,Coll}} = -1.0$, second row from top at $k_{\text{Int,Coll}} = -2.0$, third row from top at $k_{\text{Int,Coll}} = -3.0$, and bottom row at $k_{\text{Int,Coll}} = -4.0$. Each column represents day 1 (left), day 3 (middle), and day 6 (right). All other parameters are kept as in Table 1.
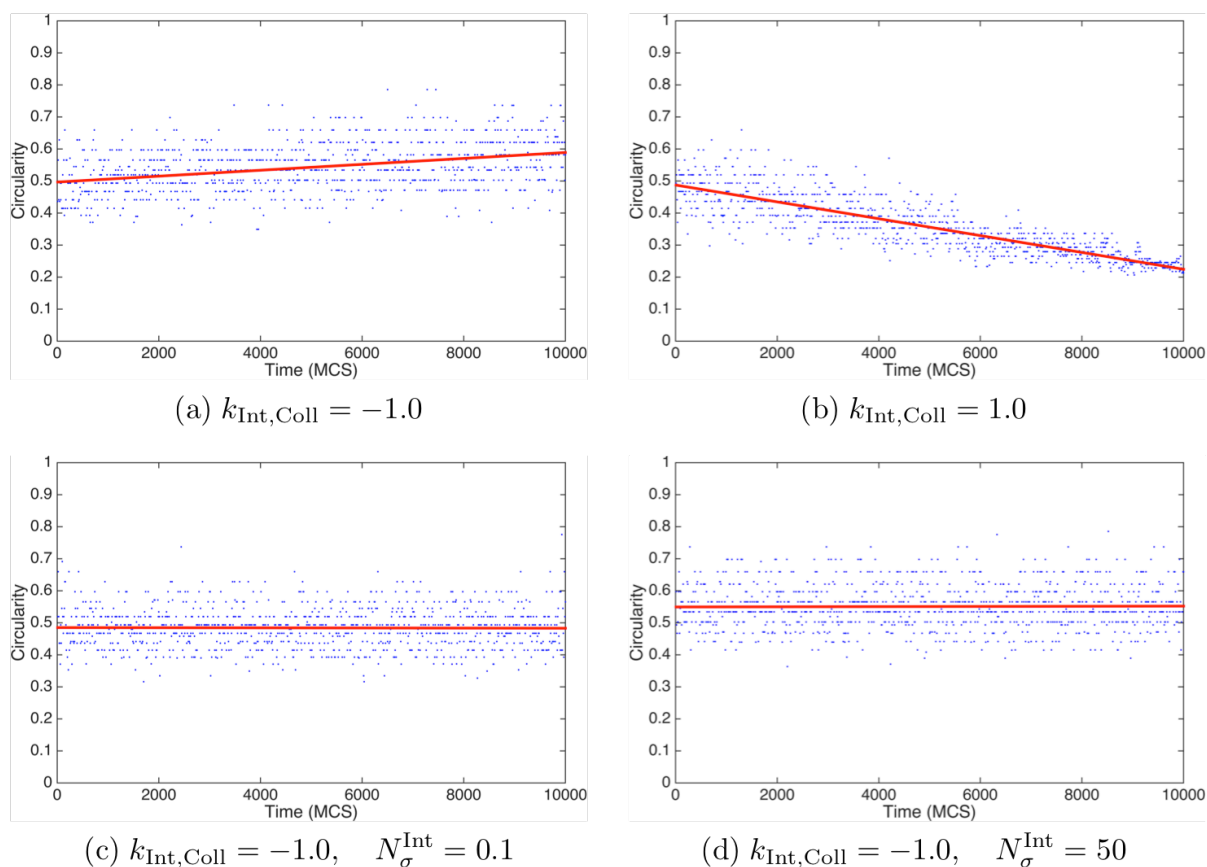
Integrative Biology Accepted Manuscript
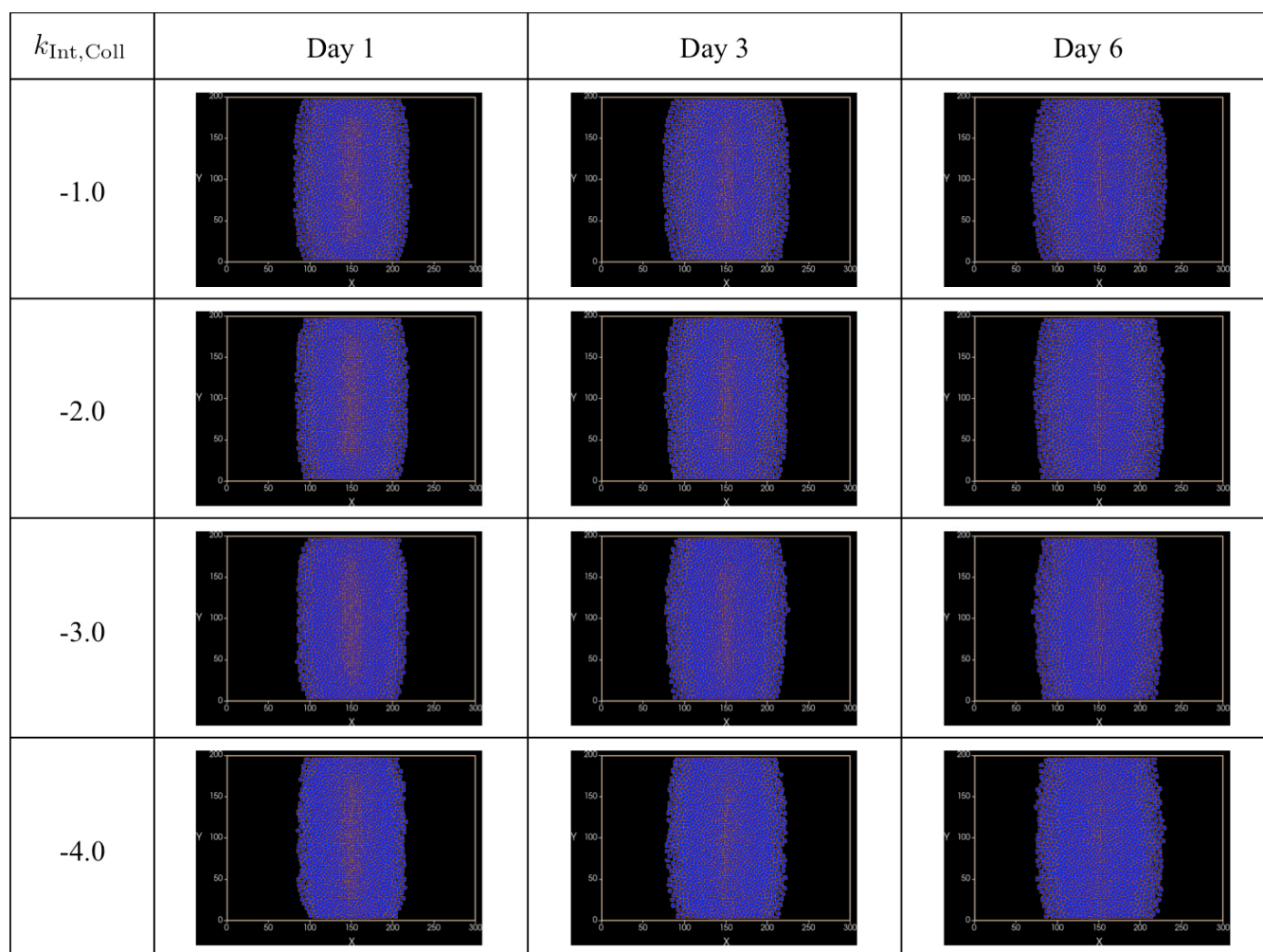
Fig. 7 Simulation results of monoculture fibroblasts with constant integrin expression. Screenshots showing results of fibroblasts with membrane fluctuation $T_{m,f} = 7$. Figures in the top row represent monoculture fibroblasts with $k_{Int,Coll} = -1.0$, the second row from the top for fibroblasts with $k_{Int,Coll} = -2.0$, the third row with $k_{Int,Coll} = -3.0$, and the bottom row with $k_{Int,Coll} = -4.0$. Each column represents day 1 (left), day 3 (middle), and day 6 (right).

(a) Keratinocyte monocultures

(b) Fibroblast monocultures
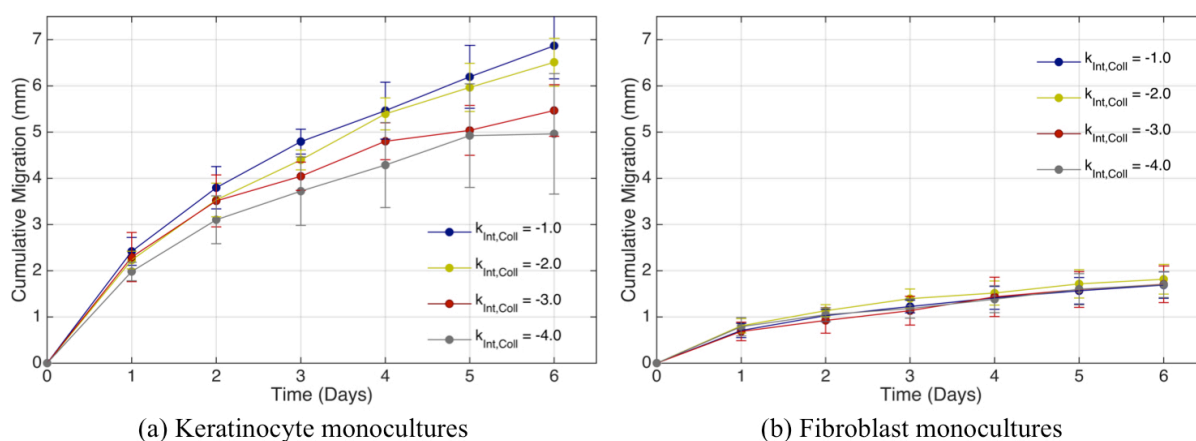
Fig. 8 Plots of average cumulative migration distances of keratinocyte (left) and fibroblast (right) monocultures. Average cumulative migration distances of monoculture simulations are plotted at $k_{Int,Coll} = -1.0$ (blue line), $k_{Int,Coll} = -2.0$ (yellow line), $k_{Int,Coll} = -3.0$ (red line), and $k_{Int,Coll} = -4.0$ (grey line).
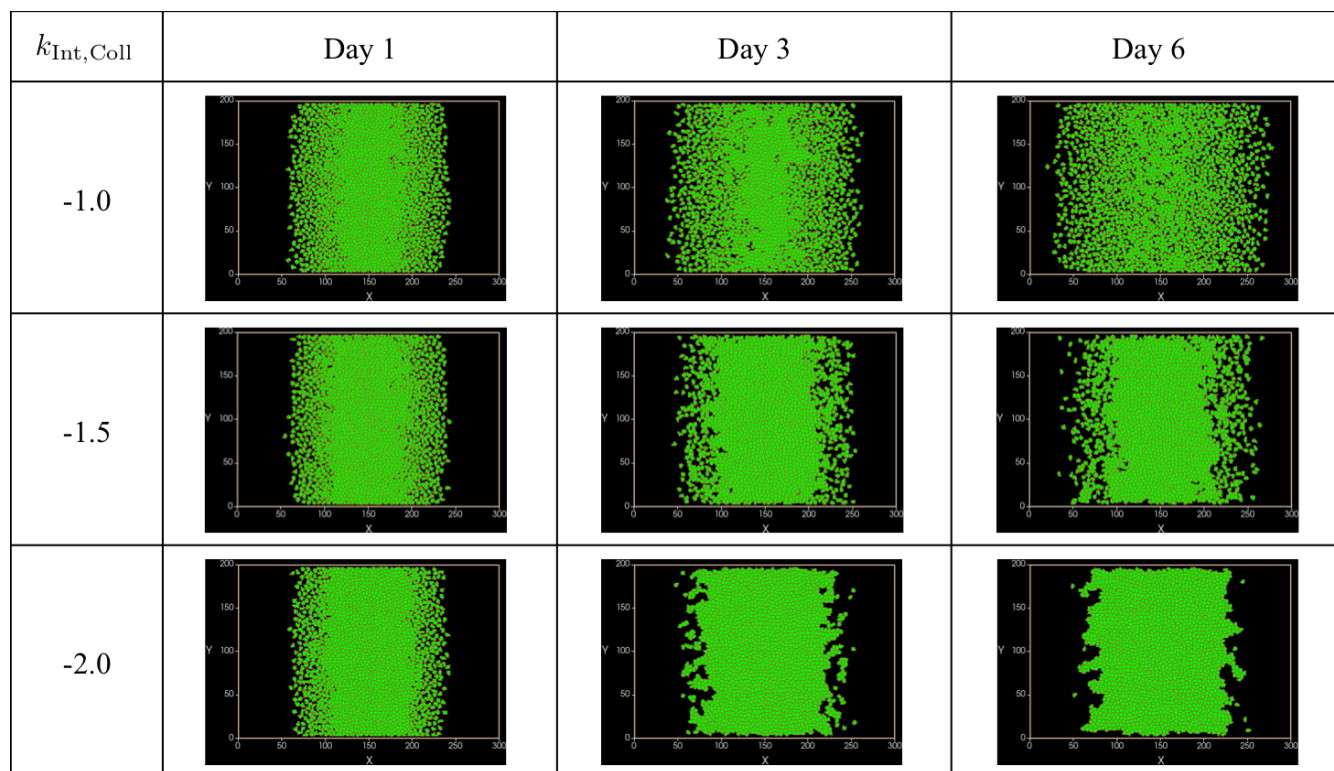
Fig. 9 Simulation results for monoculture keratinocytes with increasing integrin expression and decreasing integrin-ligand binding affinity. Screenshots showing results of keratinocytes (with membrane fluctuation $T_{m,k} = 80$) where integrin expression is varied following equation (17). The top row figures represent results with $k_{Int,Coll} = -1.0$, middle row with $k_{Int,Coll} = -1.5$, and bottom row with $k_{Int,Coll} = -2.0$. Each column represents day 1 (left), day 3 (middle), and day 6 (right).

(a) $k_{\mathrm{Int,Coll}} = -1.0$

(b) $k_{\mathrm{Int,Coll}} = 1.0$

(c) $k_{\mathrm{Int,Coll}} = -1.0, \quad N_\sigma^{\mathrm{Int}} = 0.1$

(d) $k_{\mathrm{Int,Coll}} = -1.0, \quad N_\sigma^{\mathrm{Int}} = 50$

Fig. 11 Curve fittings of cell circularity as a measure of cell motility. Figure (a) shows an increase of circularity from 0.5 to around 0.6 with negative integrin-ligand binding affinity $k_{\mathrm{Int,Coll}} = -1.0$, indicating reduced motility or cell migration speed, whereas figure (b) shows sharp decreased circularity with positive integrin-ligand binding affinity $k_{\mathrm{Int,Coll}} = 1.0$ that indicates increased cell motility. In both simulations, integrin expression was increased indefinitely from $N_\sigma^{\mathrm{Int}} = 0.1$ using equation (17). In figures (c) and (d), integrin expression is kept constant, with $N_\sigma^{\mathrm{Int}} = 0.1$ (c) and $N_\sigma^{\mathrm{Int}} = 50$ (d), where integrin-ligand binding affinity is negative.
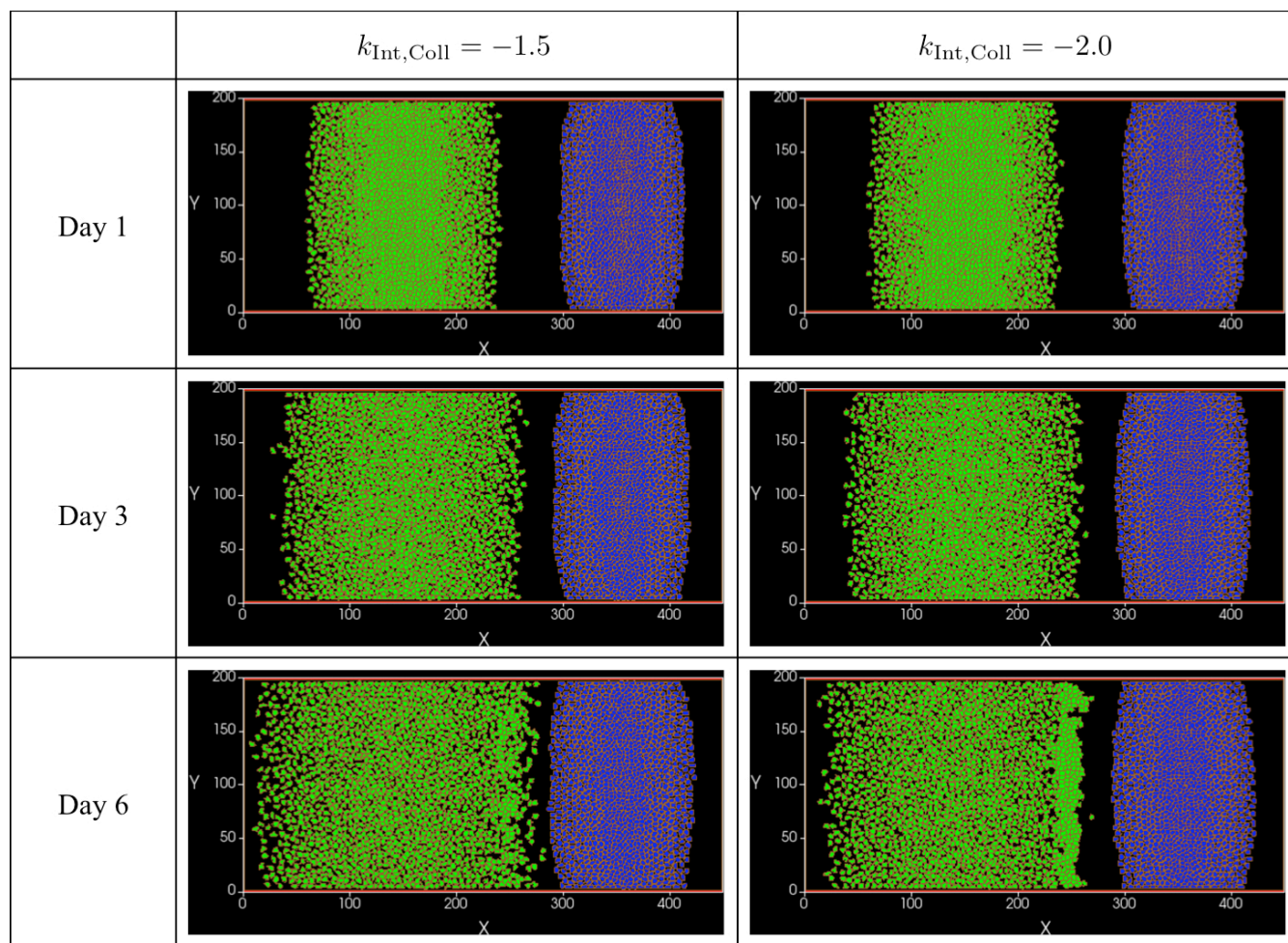
Fig. 13 Plots of co-culture simulations. Examples of co-culture simulation results, representing keratinocytes (green cells) and fibroblasts (blue cells) on day 1 (top row), day 3 (middle row), and day 6 (bottom row) with $k_{\text{Int,Coll}} = -1.5$ (left column) and $k_{\text{Int,Coll}} = -2.0$ (right column). Asymmetric migration pattern is noticeably visible for simulations with lower $k_{\text{Int,Coll}}$, such as $k_{\text{Int,Coll}} = -2.0$ on day 6 (bottom right). All parameters are as in Table 1 with $D_E = 0.25$ and $\phi = 0.2$.
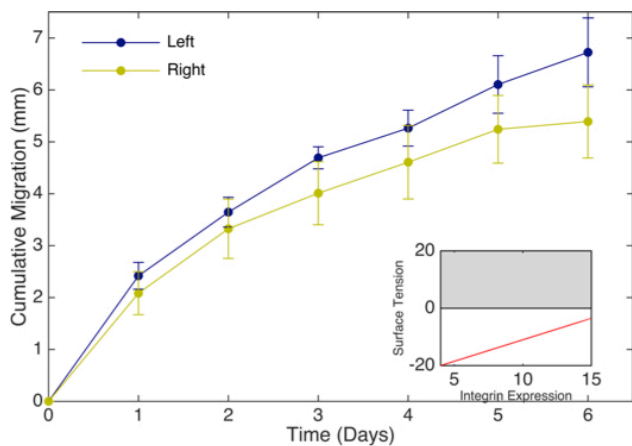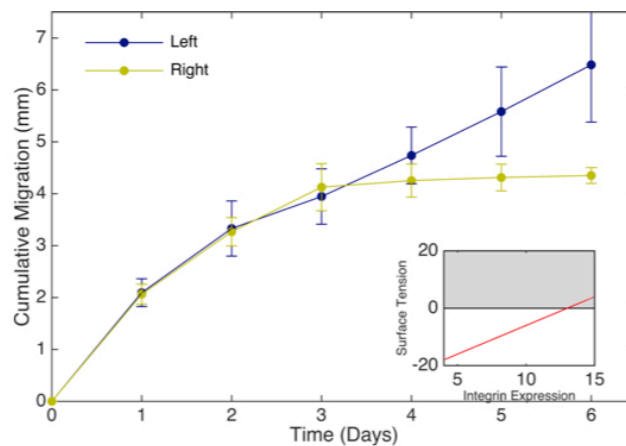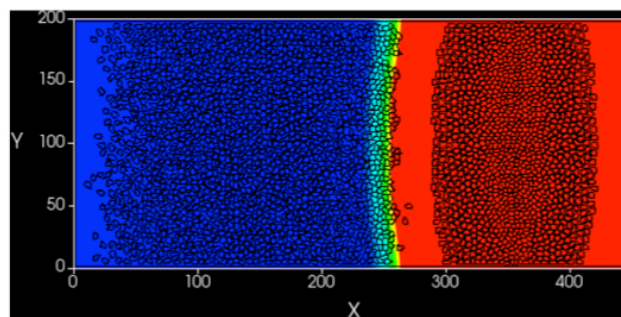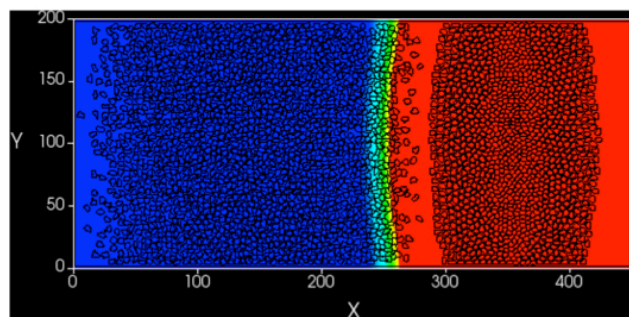
Fig. 14 Plots of average cumulative migration distances and simulation screenshots. Top row represents average cumulative distances of keratinocytes moving to the right toward fibroblasts (yellow line) and keratinocytes moving to the left or away from fibroblasts (blue line). Simulation screenshots of cells with EGF field taken on day 6 are shown in the bottom row. All parameters are as in Table 1 with $D_E = 0.25$ and $\phi = 0.2$. Left figures represent simulations with $k_{\text{Int,Coll}} = -1.5$ and right figures with $k_{\text{Int,Coll}} = -2.0$. Insert figures show surface tension variation in response to increased integrin expression of keratinocyte moving to the right.
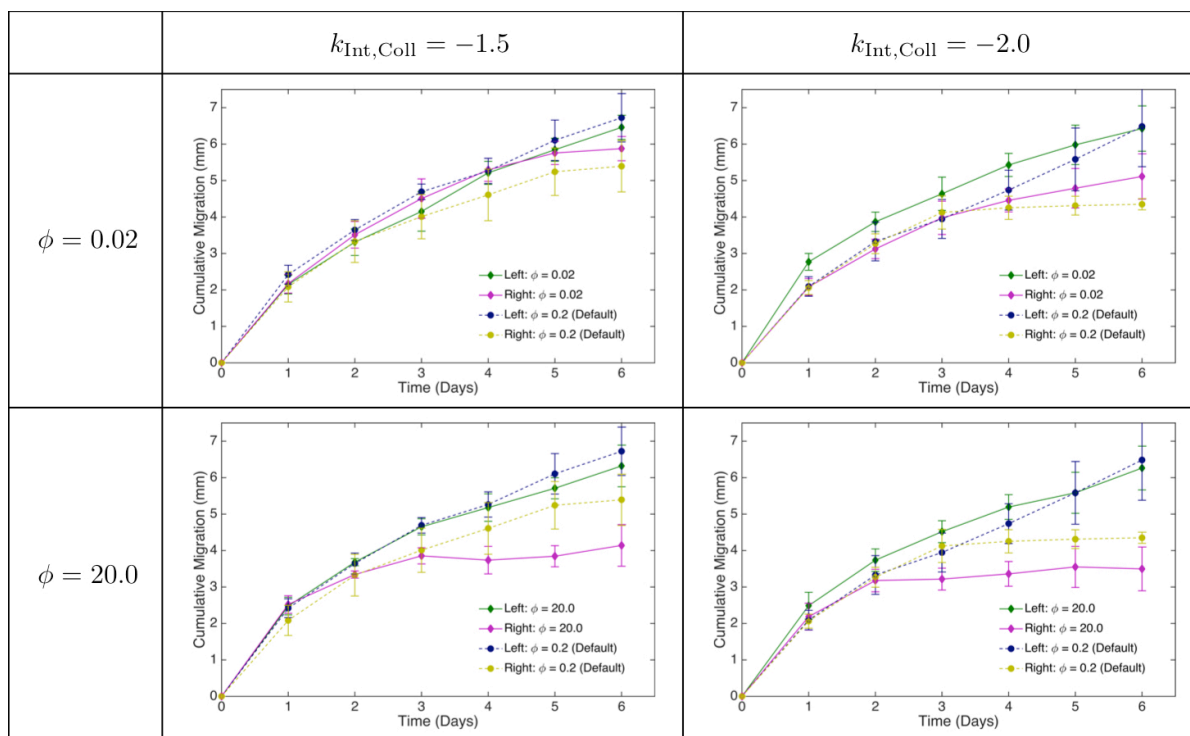
Fig. 15 Plots of average cumulative migration of keratinocytes when varying EGF secretion rate ϕ. Magenta line represents keratinocyte moving to the right or toward the fibroblasts and green line for the cell moving to the left or away from fibroblasts, when EGF secretion rate is reduced to $\phi = 0.02$ (top row) and increased to $\phi = 20.0$ (bottom row). These plots are compared with the average cumulative migration using the default secretion rate $\phi = 0.2$ (dashed yellow and blue lines) as in Figure 14.
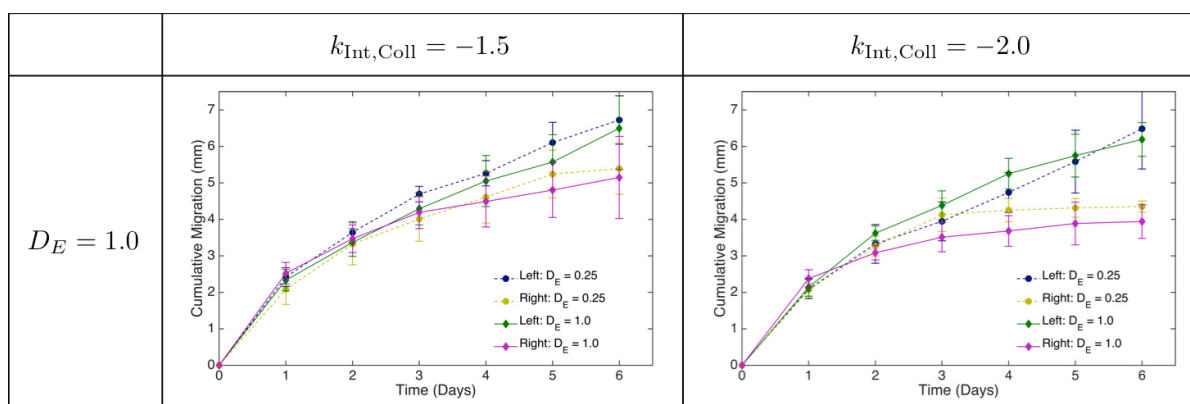
Fig. 16 Plots of average cumulative migration of keratinocytes with increasing EGF diffusion coefficient D_E. Magenta line represents keratinocyte moving to the right or toward fibroblasts and green line for keratinocyte moving to the left or away from fibroblasts at high integrin-ligand binding affinity $k_{\text{Int,Coll}} = -1.5$ (left) and lower $k_{\text{Int,Coll}} = -2.0$ (right). These plots are compared with the plots of average cumulative migration using default diffusion coefficient $D_E = 0.2$ (dashed yellow and blue lines).

Integrative Biology Accepted Manuscript
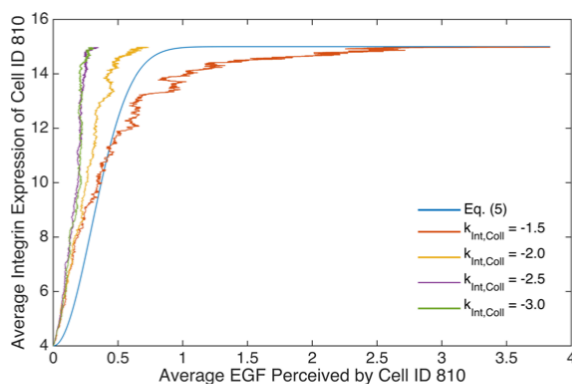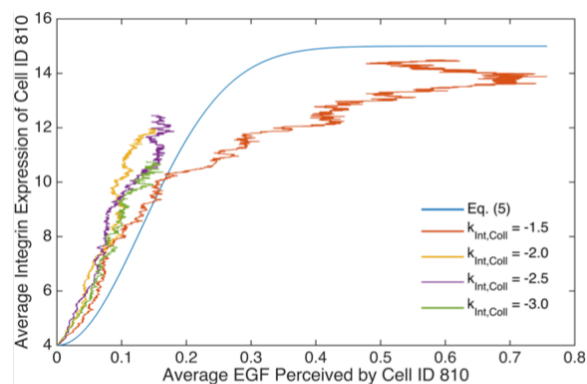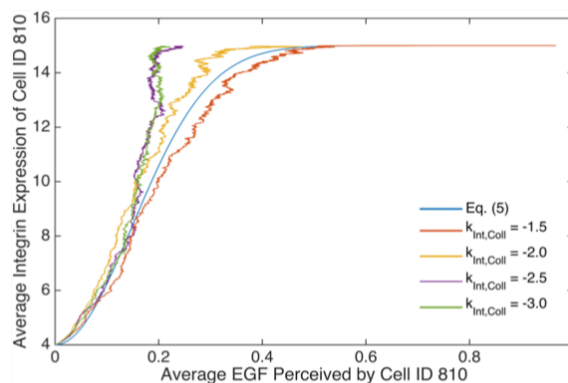
(a) Parameters in Table 1

(b) $\phi = 0.02$

(c) $D_E = 1.0$

Fig. 17 Plots of average integrin density vs EGF concentration. Average integrin expression by a keratinocyte cell migrating to the right (toward fibroblasts) as a function of average EGF concentration perceived by the same cell, identified as `Cell ID 810`, using: (a) defaults parameters in Table 1, (b) decreased EGF secretion by fibroblasts to $\phi = 0.02$, and (c) increased diffusion constant to $D_E = 1.0$. Each plot represents different $k_{Int,Coll}$ from simulation results and is compared with equation (5) (blue line).
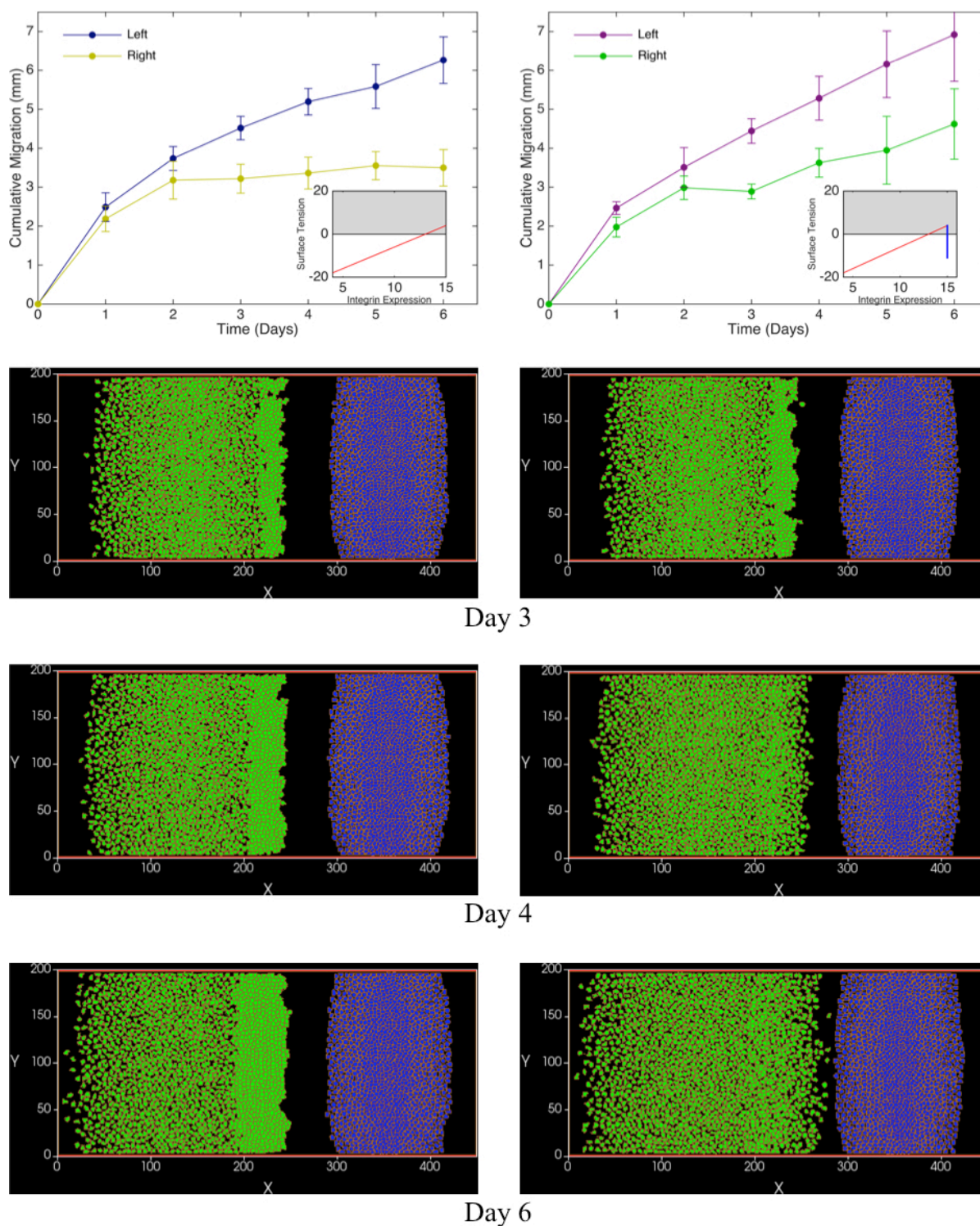
Day 3

Day 4

Day 6

Fig. 18 Results of steering $k_{Int,Coll}$ mid-simulation. Plots and screenshots on the right show the results if $k_{Int,Coll} = -2.0$ is switched to $k_{Int,Coll} = -1.0$ in the middle of simulation when it is perceived that keratinocytes moving to right undergo cell cohesion, hence, enabling cells to be motile again and restoring migration speed, compared to without steering (left figures). Both sides are simulated with high EGF secretion rate, $\phi = 20.0$.
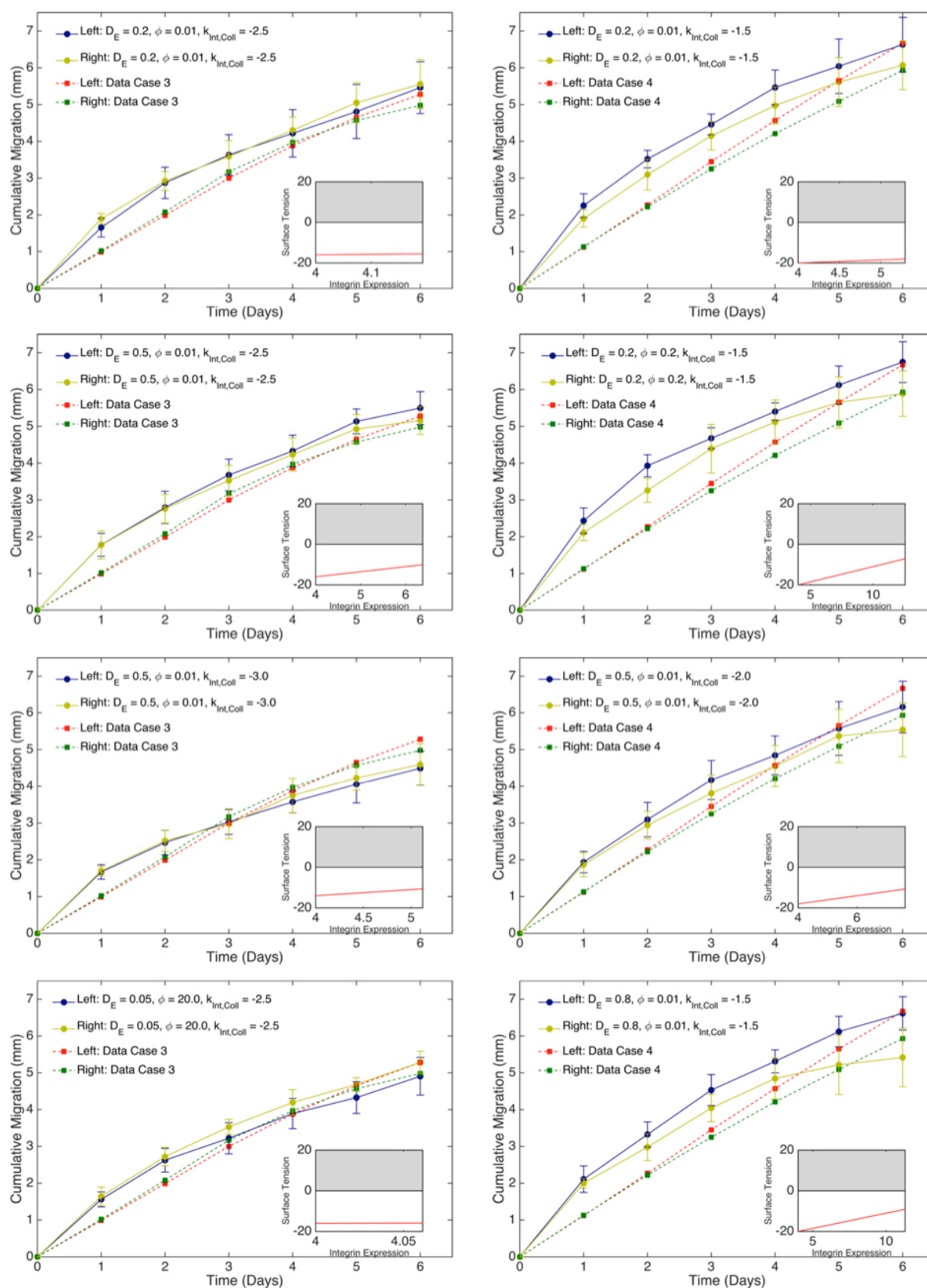
Fig. 19 Fitting of simulation results to data. Figures in the left column compare simulation results with data of co-culture experiments without EGF enhancement or case 3 as in Figure 3. Figure in the right hand column compare simulation results with data of co-culture experiments with mechanical stretch or case 4.
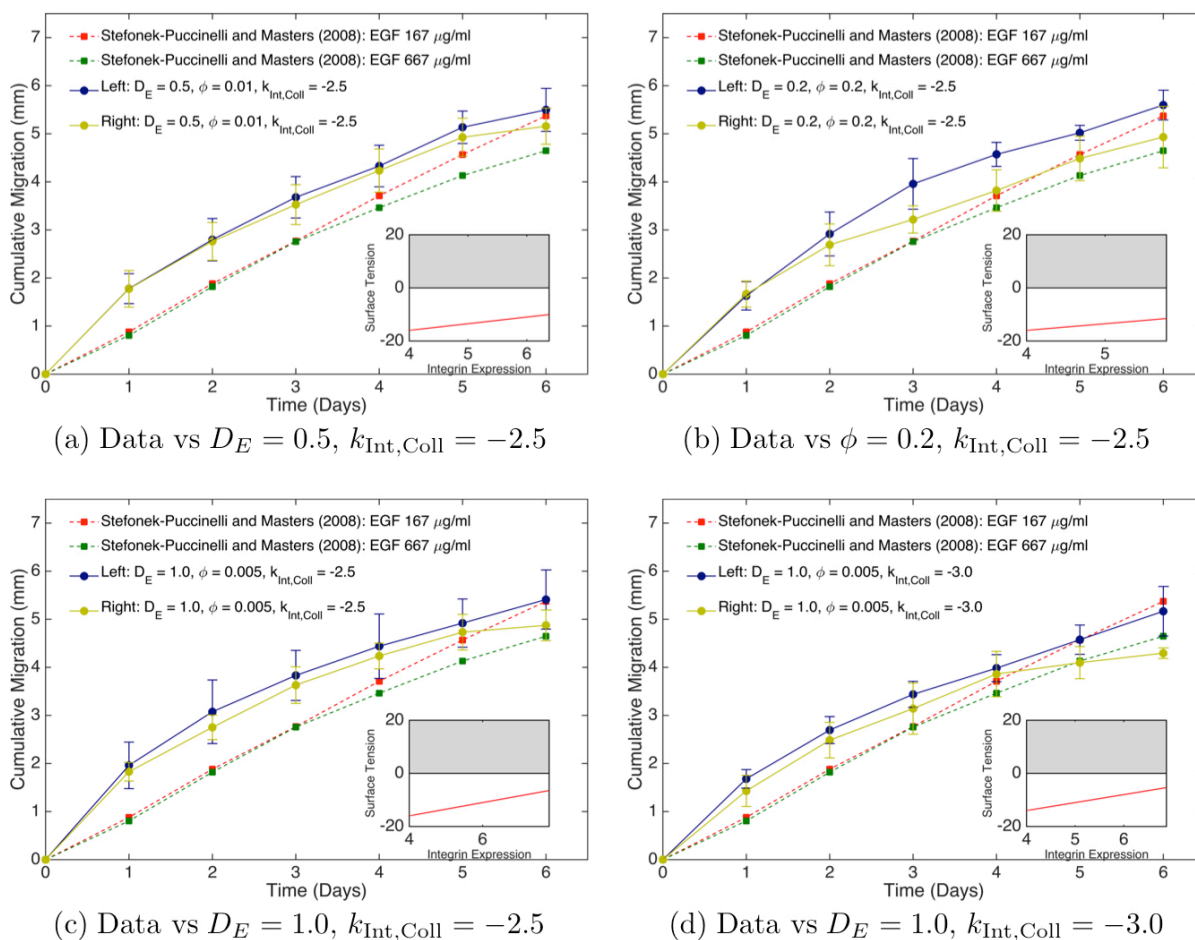
(a) Data vs $D_E = 0.5$, $k_{\text{Int,Coll}} = -2.5$

(b) Data vs $\phi = 0.2$, $k_{\text{Int,Coll}} = -2.5$

(c) Data vs $D_E = 1.0$, $k_{\text{Int,Coll}} = -2.5$

(d) Data vs $D_E = 1.0$, $k_{\text{Int,Coll}} = -3.0$

Fig. 20 Fitting of simulation results to data in[36]. Simulation results using: (a) $D_E = 0.5$ at $k_{\text{Int,Coll}} = -2.5$, (b) $\phi = 0.2$ at $k_{\text{Int,Coll}} = -2.5$, (c) $D_E = 1.0$ and $\phi = 0.005$ at $k_{\text{Int,Coll}} = -2.5$, and (d) $D_E = 1.0$ and $\phi = 0.005$ at $k_{\text{Int,Coll}} = -3.0$, are compared to experimental results[36]: Reprinted from Annals of Biomedical Engineering, Co-Immobilization of Gradient-Patterned Growth Factors for Directed Cell Migration, 36, 2008, 2121-2133, T.J. Stefonek-Puccinelli and K.S. Masters, Copyright © 2008 with permission of Springer.
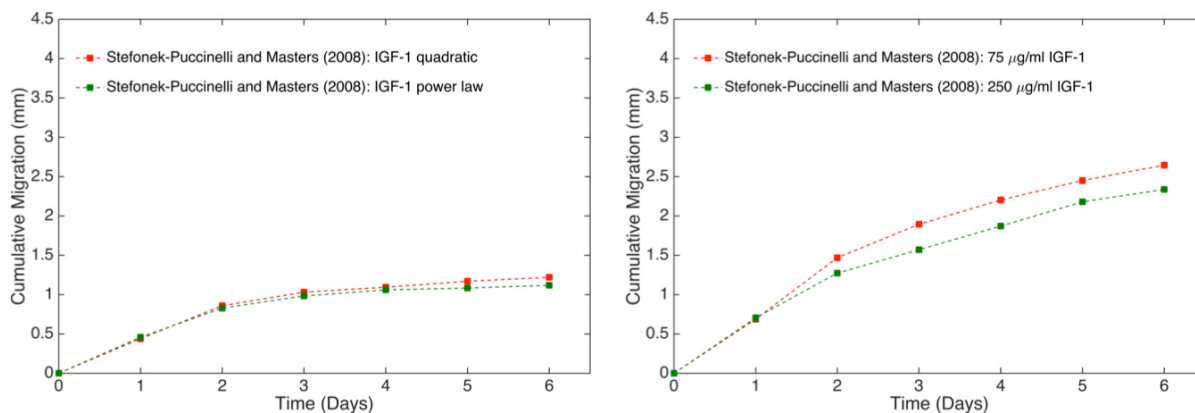

Fig. 21 Keratinocyte cumulation migration using IGF-1 in[36]. These are experimental results using IGF-1 reproduced from[36]: Reprinted from Annals of Biomedical Engineering, Co-Immobilization of Gradient-Patterned Growth Factors for Directed Cell Migration, 36, 2008, 2121-2133, T.J. Stefonek-Puccinelli and K.S. Masters, Copyright © 2008 with permission of Springer. Their results are qualitatively comparable with our results, such in Figures 15 and 16.